J. Fluid Mech. (1978), *vol.* 87, *part* 4, *pp.* 609–640
Printed in Great Britain

Ionizing argon boundary layers. Part 1. Quasi-steady flat-plate laminar boundary-layer flows

By W. S. LIU,† B. T. WHITTEN AND I. I. GLASS
Institute for Aerospace Studies, University of Toronto, Ontario, Canada M3H 5T6

(Received 17 October 1977)

Details are given of an implicit six-point finite-difference scheme for solving two-temperature, laminar, boundary-layer flows not in chemical equilibrium in ionizing argon. The analysis extends previous work by considering the radiation-energy loss and the chemical reactions due to atom–atom and electron–atom collisions in the ionizing boundary-layer and free-stream flow. Also included are variations in transport properties based on known elastic-scattering cross-sections, effects of chemical reactions, radiation-energy loss and the electric-sheath wall boundary conditions. The results are compared with dual-wavelength interferometric boundary-layer data obtained by using a Mach–Zehnder interferometer 23 cm in diameter with the UTIAS 10 × 18 cm Hypervelocity Shock Tube for shocks of initial Mach numbers $M_s \sim 13$ and 16 moving into argon at a pressure $p_0 \sim 5$ torr and temperature $T_0 \sim 297$ °K. Considering the difficulties involved in solving such complex plasma flows, satisfactory agreement was obtained between analytic and experimental total-density profiles and electron-number-density profiles for the case $M_s \sim 16$ and good agreement for $M_s \sim 13$.

1. Introduction

An understanding of boundary-layer flows in partially ionized gases is helpful in designing successful spacecraft for re-entry into the earth's atmosphere at hypersonic conditions. It also provides insight into interactions between solid surfaces and plasma flows. Despite years of research, boundary-layer flows of partially ionized gases are not fully understood experimentally or theoretically. The character of an ionizing boundary layer was described schematically by Knōōs (1968). The following characteristics are important in considering partially ionized boundary-layer flows: transport properties, interactions between the plasma and the metal (or other) surface, atomic-collision processes, chemical reactions, radiation-energy transfer and electromagnetic fields. The full boundary-layer problem is exceedingly complex, and only a few simplified cases have been treated by the early investigators. Usually, some approximations were made to suit a given problem as well as to reduce the computation costs.

In general, an ionizing gas (plasma) is composed of molecules, atoms, molecular ions, atomic ions and electrons. However, since the molecular dissociation energy is much less than the atomic ionization energy, ionization can be considered to become appreciable only after dissociation is practically complete. Therefore the mixture is assumed

† Present address: Thermalhydraulics Research Branch, Atomic Energy of Canada Ltd, Pinawa, Manitoba, Canada.

to be composed only of atoms, atomic ions and electrons. The presence of electrons in a gas introduces some features quite different from those encountered in chemical dissociation. For example, the collisional energy-transfer processes between electrons and heavy particles are relatively slow, giving rise to a possible situation where the electrons may have a temperature very different from that of the heavy particles. The extremely low mass of the electrons yields a species whose thermal conductivity can be greater than that of the other species. When such a gas is in contact with a cold surface, a space-charge sheath is formed which may affect the energy transfer to the surface. The electrons may have a higher temperature than the heavy particles near the cool surface.

A mixture of atoms, ions and electrons is uniquely described by three independent state parameters: pressure, temperature and degree of ionization. In general, an ionizing gas is in a state of thermal and chemical non-equilibrium. If thermal equilibrium is assumed (which usually cannot be expected to occur in a boundary-layer flow) the temperatures of heavy particles and electrons are equal. If chemical equilibrium is assumed then the degree of ionization can be given as a function of the local pressure and temperature via the Saha equation. If a frozen state is assumed the electron-number-density production rate becomes equal to zero. The above assumptions, which greatly simplify the solution of ionizing boundary-layer flows, were applied by some early investigators.

Many researchers have treated weakly ionized, collision-dominated, boundary-layer flows. Their main aim was to study the effects produced on the electrical characteristics of Langmuir probes. Examples are the incompressible flow of a weakly ionized gas treated by Su & Lam (1963) and the Couette flow problem studied by Chung (1963). These studies aimed at low temperature, velocity and electron number density regions. Under the assumption of thermal and chemical equilibrium, Fay & Kemp (1965) have studied the heat transfer to a shock-tube end wall for an ionizing monatomic gas and Knōōs (1968) has generalized this problem to a simple thermal Rayleigh boundary layer in an equilibrium flow. Back (1967) studied the heat transfer through a one-temperature laminar boundary layer from a partially ionized gas to a highly cooled wall for frozen and equilibrium-flow models based on a local-similarity approach. A finite-difference method was applied by Blottner (1964) to a one-temperature, non-equilibrium, laminar boundary layer in ionized air. Park (1964) analysed the frozen and equilibrium flow over a flat plate and at an axisymmetric stagnation point under similar and one-temperature assumptions and compared the results with experimental heat-transfer data. Finson & Kemp (1965) extended the theory of Fay & Kemp (1965) to stagnation-point heat transfer. For a two-temperature boundary-layer structure Camac & Kemp (1963) used a local similarity approach to study the energy transfer for a frozen flow. Sherman & Reshotko (1969) obtained the electron temperature profiles for flow in chemical equilibrium on the basis of a similar solution. Nishida & Matsuoka (1971) solved the similarity equations for a frozen flow with constant transport properties. Flat-plate boundary layers in partially ionized gases with thermal non-equilibrium and recombination for electron–ion–electron collisions were analysed by Tseng & Talbot (1971) on the basis of a similar solution and constant transport properties. Recently, Takano & Akamatsu (1975) used a finite-difference method to solve the shock-tube side-wall boundary-layer flow with constant transport properties. Honma & Komuro (1976) studied a frozen boundary-layer flow behind a moving shock

wave with variable transport properties across the boundary layer. The thermal, Rayleigh boundary-layer flow for partially ionized argon with variable transport properties was studied numerically by Mansfeld (1976) for thermal and chemical non-equilibrium and the results compared with experimental data obtained by Kuiper (1968).

These studies were usually concerned with boundary layers generated in lower temperature flows in which the heavy-particle and electron number densities were also small. As a result, the radiation-energy loss in the plasma and the ionization and recombination processes due to atom–atom collisions were neglected entirely in both the free-stream and the boundary-layer flow. Omitting the radiation-energy loss will cause serious errors when the electron number density and temperature are high. Therefore, for a boundary-layer flow generated, for example, in a shock tube by stronger shock waves ($M_s \geqslant 13$), the radiation-energy loss should be taken into account for a realistic analysis. As will be seen, the radiation loss in the shock-tube case will introduce unsteadiness into the flow induced over a stationary flat plate. This unsteadiness becomes more pronounced for higher shock Mach numbers, when the radiation loss is significant.

The importance of the inelastic atom–atom collisions with regard to ionization and recombination in the plasma will vary. When the atom and electron temperatures are not too different, the electron–atom collisions will dominate and the effect of atom–atom collisions is small. However, it is well known for the structure of ionizing shock waves (Glass & Liu 1978) that, when the atom temperature is considerably higher than the electron temperature, the atom–atom ionization process will be important. In a boundary-layer flow, the opposite casein which the atom temperature is much lower than the electron temperature can be approached. The possibility arises that atom–ion–electron recombination could become significant and should be considered.

The following difficulties arise in the analysis: (i) evaluation of the reaction-rate coefficients near the wall; (ii) the boundary conditions for the degree of ionization and electron temperature at the wall.

First, near the wall the temperature of the heavy particles is in equilibrium with the wall temperature and is usually very small compared with that at the edge of the boundary layer. Near the wall the electron number density is also very low. In this domain of low temperature and low electron number density, ionization hardly occurs. However, here the reverse chemical reaction-rate coefficients for atom–ion–electron and electron–ion–electron three-body recombinations are extremely large and difficult to evaluate.

Second, the boundary conditions for the degree of ionization and the electron temperature at the wall are usually determined from the collision-free-sheath theory. However, some authors, for example Mansfeld (1976), found that owing to the assumptions and incomplete description of the electric sheath a comparison of theoretical and experimental results would be of questionable value near the wall. Careful experiments to determine the electron number density near the wall must be done in order to check the validity of the electric-sheath theory.

The difficulty in using the finite-difference method for an ionizing non-equilibrium boundary layer lies in the stability of the scheme and in the significant computation costs. The stability criterion is difficult to evaluate for the set of strongly coupled

parabolic nonlinear partial differential equations with their boundary conditions of a mixed Neumann and Dirichlet type. In order to avoid the difficulty of stability, Mansfeld (1976) applied a backward implicit method in the time-dependent one-dimensional Rayleigh problem. However his program verges on requiring the maximum acceptable computation time.

Measurements in non-equilibrium flat-plate boundary-layer flows of ionizing argon have been reported by Tseng & Talbot (1971), Brown & Mitchner (1971) and Bredfeldt *et al.* (1967) for the regions of low temperature ($< 10\,000\,^{\circ}\mathrm{K}$) and low electron number density ($n_e \leqslant 10^{15}\,\mathrm{cm}^{-3}$). In this domain of low temperature and low electron number density, the radiation-energy loss is very small and can be neglected in both the inviscid and the viscous flow region. The edge conditions for the boundary layer were calculated from the non-radiant model. However, for the case of boundary-layer flows generated by strong moving shock waves ($M_s \geqslant 13$), the non-radiant equilibrium model cannot be applied to the inviscid region, where the radiative process is important. The radiation-energy loss was neglected in the previous comparisons with experiments.

The present paper studies analytically and experimentally flat-plate boundary-layer flows in partially ionized argon. Details are given of an implicit six-point finite-difference scheme for solving two-temperature, steady, laminar, boundary-layer flows not in chemical equilibrium in ionizing argon. The analysis includes radiation-energy losses and chemical reactions due to atom–atom and atom–electron collisions in the plasma of the inviscid and viscous flows. Variations across the boundary layer of transport properties based on known elastic-scattering cross-sections for an argon plasma are considered. The electric-sheath theory for the wall boundary conditions and the compatibility conditions for the edge of boundary layer are included in the analysis. The effects of chemical reactions, radiation-energy loss and electric-sheath theory on the boundary-layer structure are discussed. The quasi-steady flat-plate boundary-layer flows are analysed and compared with interferometric data (Whitten 1977) obtained using the UTIAS 10×18 cm Hypervelocity Shock Tube at shock Mach numbers $M_s \sim 13$ and 16 with an initial argon pressure $p_0 \sim 5$ torr. The finite-difference non-equilibrium and frozen solutions are also compared with a similarity solution for equilibrium flow.

2. Theoretical analysis

Basic equations of motion and thermal properties of an argon plasma

The following basic assumptions are made.

(i) In a mixture of atoms, ions and electrons, each species has a near-Maxwellian velocity distribution with an appropriate temperature. This condition for the electrons and ions implies a Larmor radius much greater than the mean free path or that the elastic collision frequency is very large.

(ii) The gas is singly ionized and the electron number density is equal to the ion number density, or the plasma is quasi-neutral. Therefore the effects of electric and magnetic fields on the boundary-layer structure are neglected. The essential requirement for quasi-neutrality is that the Debye length is much smaller than the boundary-layer thickness. The ambipolar character of the diffusion process results from this assumption provided that no electric currents cross the boundary.

(iii) The atom and ion temperatures are equal, or atoms and ions have the same velocity. This assumption can be justified since the mass of the ions is almost equal to that of the atoms, and therefore only a few collisions between atoms and ions are necessary to reach a common temperature.

A partially ionized monatomic gas or plasma which consists of a mixture of atoms, ions and electrons is considered. For each species the macroscopic balance equations can be expressed by using the plasma macroscopic properties (Appleton & Bray 1964). Following the above assumptions, the basic equations of motion for a steady boundary-layer flow of an ionizing gas are given by

$$\frac{\partial}{\partial x}(\rho u)+\frac{\partial}{\partial y}(\rho v)=0 \quad \text{(mass of plasma)}, \tag{1}$$

$$\rho u\frac{\partial u}{\partial x}+\rho v\frac{\partial u}{\partial y}=-\frac{dp}{dx}+\frac{\partial}{\partial y}\left(\mu\frac{\partial u}{\partial y}\right) \quad \text{(momentum of plasma)}, \tag{2}$$

$$\rho u\frac{\partial H}{\partial x}+\rho v\frac{\partial H}{\partial y}=-\frac{\partial}{\partial y}(q_c+q_d)+\frac{\partial}{\partial y}\left(\mu u\frac{\partial u}{\partial y}\right)-Q_R \quad \text{(energy of plasma)}, \tag{3}$$

$$\rho u\frac{\partial \alpha}{\partial x}+\rho v\frac{\partial \alpha}{\partial y}=-\frac{\partial}{\partial y}(\rho_i V_i)+m_a\dot{n}_e \quad \text{(electron production rate)}, \tag{4}$$

$$\rho u\frac{\partial}{\partial x}(\alpha C_p T_e)+\rho v\frac{\partial}{\partial y}(\alpha C_p T_e)=u\frac{\partial p_e}{\partial x}+(v+V_i)\frac{\partial p_e}{\partial y}-\frac{\partial}{\partial y}(q_{ce}+q_{de})+Q_{el}+Q_{inel} \quad \text{(electron energy)}. \tag{5}$$

Here u and v are the mean mass velocities of plasma in the x and y directions, x being along the plate surface and y normal to it, ρ is the plasma density, p the plasma pressure, μ the plasma viscosity coefficient, H the total enthalpy of the plasma, q_c the plasma heat-conduction flux, q_d the plasma diffusive-energy flux, Q_R the plasma radiation-energy loss per unit volume, α the degree of ionization, V_i the ion diffusive velocity relative to v, m_a the mass of an atom, $\dot{n}_e$ the electron-number-density production rate, Q_{el} the rate at which thermal energy is given to free electrons by elastic collisions, Q_{inel} the inelastic energy-transfer rate, p_e the electron pressure, T the temperature, and subscripts e and i denote electron and ion encounters, respectively. The following relations apply:

$$\left.\begin{aligned}
&\rho = m_a(n_a+n_e),\\
&p = (n_a+n_e)\,k_B T_a+n_e k_B T_e, \quad C_p=\tfrac{5}{2}R \quad \text{(defined as a constant for convenience)},\\
&H = C_p(T_a+\alpha T_e)+RT_I\alpha+\tfrac{1}{2}u^2,\\
&\alpha = n_e/(n_a+n_e), \quad R=k_B/m_a,\\
&q_c = -(\lambda_a+\lambda_i)\,\partial T_a/\partial y-\lambda_e\,\partial T_e/\partial y, \quad q_{ce}=-\lambda_e\,\partial T_e/\partial y,\\
&q_d = \rho_i V_i(RT_I+C_p T_e), \quad q_{de}=C_p T_e\rho_i V_i,\\
&\rho_i V_i = -\rho D_a\left[\frac{\partial \alpha}{\partial y}+\frac{\alpha(1-\alpha)}{1+\alpha T_e/T_a}\frac{\partial}{\partial y}\left(\frac{T_e}{T_a}\right)\right], \quad p_e=n_e k_B T_e,
\end{aligned}\right\} \tag{6}$$

where the subscript a denotes atom encounters, T_I is the ionization temperature, n the

number density, R the gas constant, λ the thermal conductivity, D_a the ambipolar diffusion coefficient and k_B the Boltzmann constant.

The rate Q_R of radiant-energy loss per unit volume of a plasma consists of the rates of energy loss through continuum radiation and line radiation. In order to simplify the calculation, these two rates are assumed to be equal for the argon plasma; this assumption has been discussed by Glass & Liu (1978). Under the assumption of local-temperature equilibrium, Q_R is given by

$$Q_R = \frac{128\pi^{\frac{3}{2}}e^6}{3\times 6^{\frac{1}{2}}m_e^{\frac{3}{2}}c^3hk_B^{\frac{1}{2}}}\frac{n_e^2}{T_e^{\frac{1}{2}}}(h\nu_c + k_BT_e)\bar{g}Z_{\text{eff}}^2, \tag{7}$$

where e is the electron charge, h is Planck's constant, c is the speed of light, ν_c is the cut-off frequency, $\bar{g}$ is the Gaunt factor and Z_{eff} is the effective nuclear charge.

The shock Mach numbers considered here are not extremely high; consequently precursor radiation is neglected. The plasma is essentially optically thin, therefore reabsorption of radiation-energy loss is also neglected.

It has been shown (Petschek & Byron 1957) that excitation to the first state is rate controlling for the overall ionization process. Consequently, the following reactions are considered for the collisional ionization processes:

$$\mathrm{Ar} + \mathrm{Ar} \underset{k_{ra}}{\overset{k_{fa}}{\rightleftharpoons}} \mathrm{Ar}^+ + \mathrm{Ar} + \mathrm{e},$$

$$\mathrm{Ar} + \mathrm{e} \underset{k_{re}}{\overset{k_{fe}}{\rightleftharpoons}} \mathrm{Ar}^+ + \mathrm{e} + \mathrm{e},$$

where k_f and k_r are forward and reverse rate coefficients. From the two-temperature two-step model of Hoffert & Lien (1967), the electron-number-density production rate $\dot{n}_e$ can be written as

$$\dot{n}_e = (\dot{n}_e)_a + (\dot{n}_e)_e, \tag{8a}$$

where

$$(\dot{n}_e)_a = k_{fa}n_a^2 - k_{ra}n_an_e^2, \quad (\dot{n}_e)_e = k_{fe}n_an_e - k_{re}n_e^3. \tag{8b}$$

The elastic energy-transfer rate Q_{el} is the sum of the rates of thermal energy given to the free electrons by electron–atom and electron–ion elastic collisions:

$$Q_{el} = 3n_e(m_e/m_a)(\nu_{ea} + \nu_{ei})k_B(T_a - T_e), \tag{9}$$

where ν_{ea} and ν_{ei} are elastic collision frequencies due to electron–atom and electron–ion encounters, respectively.

The inelastic energy-transfer rate Q_{inel} is the sum of the rates of thermal energy given to the free electrons by electron–atom and electron–ion–electron inelastic collisions and by bremsstrahlung. The latter is neglected in the boundary-layer flow since it is small compared with the former. For a two-step model,

$$Q_{inel} = -k_BT_I(\dot{n}_e)_e, \tag{10}$$

where the term for the creation energy of electrons due to atom–atom ionization collisions is very small and can be neglected.

In order to simplify the present analysis, two approximations are made for the boundary-layer flows: (i) that $T_e \simeq T_a$ in the calculation of D_a in $\rho_iV_i \approx -\rho D_a\,\partial\alpha/\partial y$ and (ii) that $\mathbf{v}\cdot\nabla p_e \approx 0$. Approximation (i) has been widely accepted by many authors in the analysis of two-temperature boundary-layer flows of ionizing gases when computing the value of D_a [see (16)]. Approximation (ii) has been used by Chung & Mullen

(1963) and Takano & Akamatsu (1975) since $\mathbf{v}\,.\,\nabla p_e$ is small compared with the other terms on the right-hand side of (5). For example,

$$\rho v \frac{\partial}{\partial y}(\alpha C_p T_e) \approx 2{\cdot}5v\frac{\partial p_e}{\partial y}, \quad \frac{\partial}{\partial y} q_{de} \gg (v+V_i)\frac{\partial p_e}{\partial y}.$$

The elastic-scattering cross-sections are used in the determination of the transport properties of ionizing gases. The average atom–atom elastic-collision cross-section σ_{aa} is obtained from the values of the viscosity coefficient given by Amdur & Mason (1958). At high temperatures $\mu \approx 31 \times 10^{-7} T_a^{\frac{1}{2}}$ g/cm s, which corresponds to

$$\sigma_{aa} = 1{\cdot}7 \times 10^{-14}/T_a^{0{\cdot}25} \text{ cm}^2. \tag{11}$$

Experimental data compiled by Fay (1962) show

$$\sigma_{ai} = 2{\cdot}45 \times 10^{-14}/T_a^{0{\cdot}90} \text{ cm}^2. \tag{12}$$

The average momentum-transfer cross-sections between electrons and atoms, σ_{ea}, and between electrons and electrons, σ_{ee}, used by Glass & Liu (1978) in the analysis of argon shock-wave structure are adopted here. The average elastic-scattering cross-section σ_{ii} between ions and ions is given by

$$\sigma_{ii} = \frac{2\pi e^4}{9(k_B T_a)^2} \ln\left(\frac{9k_B^3 T_a^3}{4\pi e^6 n_e}\right). \tag{13}$$

Since $T_e/m_e \gg T_a/m_a$, the electron temperature is the relevant temperature in the calculation of the ion–electron collision cross-section; therefore

$$\sigma_{ee} = \sigma_{ei} = \frac{2\pi e^4}{9(k_B T_e)^2} \ln\left(\frac{9k_B^3 T_e^3}{4\pi e^6 n_e}\right). \tag{14}$$

The kinetic theory of gases provides a means of estimating the transport coefficients of a partially ionized gas. Here the mixture rule of Fay & Kemp (1965) is applied. For example, the viscosity of a plasma is given by

$$\mu = \frac{5\pi}{32}\frac{m_a U_a}{\sigma_{aa}} \frac{1 + l\dfrac{1 + l(\sigma_{ai}/\sigma_{aa})}{(\sigma_{ai}/\sigma_{aa}) + l(\sigma_{ii}/\sigma_{aa})}}{1 + l(\sigma_{ai}/\sigma_{aa})}, \tag{15}$$

where

$$l = \alpha/(1-\alpha), \quad U_a = (8k_B T_a/\pi m_a)^{\frac{1}{2}}.$$

The ambipolar diffusion coefficient D_a is given approximately by

$$D_a \approx \frac{0{\cdot}75}{2n_e + n_a}\left(\frac{\pi k_B T_a}{m_a}\right)^{\frac{1}{2}} \Big/ \sigma_{ai}. \tag{16}$$

The thermal conduction coefficients for atoms, ions and electrons may be written as (Jaffrin 1965)

$$\lambda_a = \frac{75k_B}{64\sigma_{aa}}\left(\frac{\pi k_B T_a}{m_a}\right)^{\frac{1}{2}}\left(1 + \frac{n_e\sigma_{ai}}{n_a\sigma_{aa}}\right)^{-1}, \tag{17}$$

$$\lambda_i = \frac{75k_B n_e}{64\sigma_{ai} n_a}\left(\frac{\pi k_B T_a}{m_a}\right)^{\frac{1}{2}}\left(1 + \frac{n_e\sigma_{ii}}{n_a\sigma_{ai}}\right)^{-1}, \tag{18}$$

$$\lambda_e = \frac{75k_B}{64\sigma_{ee}(1+2^{\frac{1}{2}})}\left(\frac{\pi k_B T_e}{m_e}\right)^{\frac{1}{2}}\left(1 + \frac{2^{\frac{1}{2}} n_a\sigma_{ea}}{(1+2^{\frac{1}{2}})n_e\sigma_{ee}}\right)^{-1}. \tag{19}$$

The forward rate coefficients k_f in (8*b*) can be obtained by computing the collision rate between two particles. Only the energy dependence of the inelastic cross-section

near the threshold energy is important in the calculation of the rate coefficients. The general forms for the leading threshold behaviour of inelastic cross-sections can be obtained from classical scattering theory or Wigner's R-matrix theory (Eu & Liu 1975). For the present analysis, a reasonably good approximation of the inelastic cross-section is given by the linear relationship

$$\sigma^*_{ab}(\epsilon) = \begin{cases} S^*_{ab}(\epsilon - \epsilon^*) & \text{for} \quad \epsilon \geqslant \epsilon^*, \\ 0 & \text{for} \quad \epsilon < \epsilon^*, \end{cases} \tag{20}$$

where ϵ is the kinetic energy (in centre-of-mass co-ordinates) of particle b (b can be either an atom or an electron), ϵ^* is the first excitational energy of particle a and S^*_{ab} is the first excitational collision cross-section constant.

From a comparison of our analytical and experimental results for argon shock-wave structure, we found that $S^*_{aa} = 1{\cdot}0 \times 10^{-19}\,\mathrm{cm^2/eV}$ (Glass & Liu 1978). A more recent electron–atom excitational cross-section constant $S^*_{ae} = 4{\cdot}9 \times 10^{-18}\,\mathrm{cm^2/eV}$ for argon obtained by Zapesochnyi & Feltsan (1966) is used here. Therefore k_{fa} and k_{fe} yield

$$k_{fa}(T_a) = 1{\cdot}4 \times 10^{-20} T_a^{1{\cdot}5} (T^*/T_a + 2) \exp(-T^*/T_a)\,\mathrm{cm^3/s}, \tag{21}$$

$$k_{fe}(T_e) = 2{\cdot}63 \times 10^{-16} T_e^{1{\cdot}5} (T^*/T_e + 2) \exp(-T^*/T_e)\,\mathrm{cm^3/s}, \tag{22}$$

where $T^* = 134\,000\,^\circ\mathrm{K}$ is the first excitational temperature of the argon atom.

Hoffert & Lien (1967) used a chemical-equilibrium concept to determine k_{ra} and k_{re} for the present case of chemical non-equilibrium. However, for low temperatures these results are not valid and the ionic-recombination theory based on the classical electron-impact cross-section is needed. In order to avoid the difficulty of determination of the reverse reaction-rate coefficients, a critical temperature T_c is defined which separates the regions of high and low temperature. This critical temperature can be obtained by ensuring the continuity of the rate coefficients at T_c. For electron-catalysed reactions, Hinnov & Hirschberg (1962) have obtained an empirical relation for the reverse reaction-rate coefficient at low temperatures ($T_e \leqslant 4000\,^\circ\mathrm{K}$). The following reverse reaction-rate coefficient k_{re} for electron-catalysed reactions is used:

$$k_{re}(T_e) = \begin{cases} 9{\cdot}03 \times 10^{-33} (T^*/T_e + 2) \exp[(T_I - T^*)\,T_e]\,\mathrm{cm^6/s} & \text{for} \quad T_e \geqslant T_c, \\ 1{\cdot}09 \times 10^{-8} T_e^{-4{\cdot}5}\,\mathrm{cm^6/s} & \text{for} \quad T_e \leqslant T_c, \end{cases} \tag{23}$$

where $T_c \sim 3100\,^\circ\mathrm{K}$.

For atom-catalysed reactions, a similar procedure can be applied. However, there is no available empirical relation for k_{ra} at temperatures T_a below $3000\,^\circ\mathrm{K}$. At the same time, the chemical-equilibrium concept used to determine k_{ra} by Hoffert & Lien (1967) is in serious error when the electron temperature is considerably different from the atom temperature. In order to avoid too large a value of k_{ra} at low atom temperatures, the following forms are adopted (Glass & Liu 1978):

$$k_{ra}(T_a) = \begin{cases} 4{\cdot}83 \times 10^{-37} (T^*/T_a + 2) \exp[(T_I - T^*)/T_a]\,\mathrm{cm^6/s} & \text{for} \quad T_a \geqslant T_c, \\ 4{\cdot}83 \times 10^{-37} (T^*/T_c + 2) \exp[(T_I - T^*)/T_c]\,\mathrm{cm^6/s} = \text{constant} & \text{for} \quad T_a < T_c. \end{cases} \tag{24}$$

The physical meaning of the cut-off of k_{ra} at low temperatures is that at low T_a the reverse atom–atom reaction rate is frozen at some particular rate and the re-excitation from the first excited state is not rate controlling for atom–atom collisions. In general, the reaction rates due to atom–atom collisions are very small compared with those due

to electron–atom collisions for atom temperatures below about 15 000 °K. Therefore atom-catalysed reactions can be neglected for $T_a \leqslant 15\,000$ °K in a flat-plate boundary-layer analysis where the flow has cooled significantly. However, for the case of a shock-tube side-wall boundary layer near the shock front, where the atom temperature is large ($\sim 25\,000$ °K), atom-catalysed reactions are more important than electron-catalysed reactions and k_{ra} must be retained. Byron, Stabler & Bortz (1962) have shown that for the low-temperature case de-excitation from other than the first-excited state can be rate controlling in the recombination process. For the present two-step model, the approximation made in (24) is necessary in order to avoid the unknown physical effects due to a very large value of k_{ra}. It is also worth noting that a large value of k_{ra} destabilizes the finite-difference scheme.

Transformed basic equations

The following similarity co-ordinates are introduced:

$$\xi(x) = \int_0 \rho_\delta \mu_\delta u_\delta y \, du \, dx, \quad \eta(x,y) = \frac{u_\delta}{(2\xi)^{\frac{1}{2}}} \int_0 \rho \, dy, \tag{25}$$

where the subscript δ denotes the edge of the boundary layer. The following characteristic times are defined for flow, forward atom–atom reactions, reverse atom–atom reactions, forward electron–atom reactions, reverse electron–atom reactions, elastic-energy transfer and radiative processes respectively:

$$\tau_u = \frac{2\xi}{\rho_\delta \mu_\delta u_\delta^2}, \quad \tau_{fa} = \frac{n_{e\delta}}{k_{fa}(T_{a\delta})\, n_{a\delta}^2}, \quad \tau_{ra} = \frac{1}{k_{ra}(T_{a\delta})\, n_{a\delta}\, n_{e\delta}}, \quad \tau_{fe} = \frac{1}{k_{fe}(T_{e\delta})\, n_{a\delta}},$$

$$\tau_{re} = \frac{1}{k_{re}(T_{e\delta})\, n_{e\delta}^2}, \quad \tau_{el} = \frac{1}{\frac{6}{5}(m_e/m_a)\,(\nu_{ea\delta} + \nu_{ei\delta})}, \quad \tau_R = \frac{\rho_\delta C_p T_{a\delta}}{Q_{R\delta}}.$$

The following non-dimensional quantities are defined:

$$\tau = T_{e\delta}/T_{a\delta}, \quad \epsilon_{fa} = \tau_u/\tau_{fa}, \quad \epsilon_{ra} = \tau_u/\tau_{ra}, \quad \epsilon_{fe} = \tau_u/\tau_{fe},$$

$$\epsilon_{re} = \tau_u/\tau_{re}, \quad \epsilon_{el} = \tau_u/\tau_{el}, \quad \epsilon_R = \tau_u/\tau_R,$$

$$\phi_{fa} = \frac{\rho}{\rho_\delta} \frac{\theta^{1\cdot5}}{(1-\alpha_\delta)^2} \frac{1/\theta + 2T_{a\delta}/T^*}{1 + 2T_{a\delta}/T^*} \exp\left[-\frac{T^*}{T_{a\delta}}\left(\frac{1}{\theta} - 1\right)\right],$$

$$\phi_{ra} = \left(\frac{\rho}{\rho_\delta}\right)^2 \frac{1}{1-\alpha_\delta} \frac{1/\theta + 2T_{a\delta}/T^*}{1 + 2T_{a\delta}/T^*} \exp\left[\frac{(T_I - T^*)}{T_{a\delta}}\left(\frac{1}{\theta} - 1\right)\right],$$

$$\phi_{fe} = \frac{\rho}{\rho_\delta} \frac{\Theta^{1\cdot5}}{1-\alpha_\delta} \frac{1/\Theta + 2T_{e\delta}/T^*}{1 + 2T_{e\delta}/T^*} \exp\left[-\frac{T^*}{T_{e\delta}}\left(\frac{1}{\Theta} - 1\right)\right],$$

$$\phi_{re} = \begin{cases} \left(\dfrac{\rho}{\rho_\delta}\right)^2 \dfrac{1/\Theta + 2T_{e\delta}/T^*}{1 + 2T_{e\delta}/T^*} \exp\left[\dfrac{(T_I - T^*)}{T_{e\delta}}\left(\dfrac{1}{\Theta} - 1\right)\right] & \text{for } \Theta \geqslant \Theta_c, \\ \left(\dfrac{\rho}{\rho_\delta}\right)^2 \Theta^{-4\cdot5} & \text{for } \Theta < \Theta_c, \end{cases}$$

$$\phi_{el} = \frac{\nu_{ea} + \nu_{ei}}{\nu_{ea\delta} + \nu_{ei\delta}}, \quad \phi_R = \frac{1}{\Theta^{\frac{1}{2}}} \frac{h\nu_c + k_B \Theta T_{e\delta}}{h\nu_c + k_B T_{e\delta}} z^2,$$

$$\Theta_c = T_c/T_{e\delta},$$

where

$$\nu_{ea} = n_a \sigma_{ea} (8k_B T_e/\pi m_e)^{\frac{1}{2}},$$

$$\nu_{ei} = n_e \sigma_{ei} (8k_B T_e/\pi m_e)^{\frac{1}{2}}.$$

The transformed equations for plasma momentum, electron species, atom temperature and electron temperature become

$$[Cf'']'+ff''+\beta_f\left[\frac{\rho_\delta}{\rho}-f'^2\right]=2\xi\left[f'\frac{\partial f'}{\partial\xi}-\frac{\partial f}{\partial\xi}f''\right], \tag{26}$$

$$\left[\frac{C}{Sc}z'\right]'+fz'-\beta_z zf'+\epsilon_{fa}\phi_{fa}(1-\alpha_\delta z)^2-\epsilon_{ra}\phi_{ra}z^2(1-\alpha_\delta z)$$
$$+\epsilon_{fe}\phi_{fe}z(1-\alpha_\delta z)-\epsilon_{re}\phi_{re}z^3=2\xi\left[f'\frac{\partial z}{\partial\xi}-\frac{\partial f}{\partial\xi}z'\right], \tag{27}$$

$$\left[\frac{C}{Pr}\theta'\right]'+f\theta'+\frac{u_\delta^2}{C_pT_{a\delta}}Cf''^2-\beta_{T_a}\theta f'-\beta_f\frac{u_\delta^2}{C_pT_{a\delta}}\frac{\rho_\delta}{\rho}f'-\epsilon_{el}\phi_{el}\alpha_\delta z(\theta-\tau\Theta)-\epsilon_R\phi_R\frac{\rho}{\rho_\delta}$$
$$-\frac{2}{5}\frac{T_I}{T_{a\delta}}\alpha_\delta[\epsilon_{fa}\phi_{fa}(1-\alpha_\delta z)^2-\epsilon_{ra}\phi_{ra}z^2(1-\alpha_\delta z)]=2\xi\left[f'\frac{\partial\theta}{\partial\xi}-\frac{\partial f}{\partial\xi}\theta'\right], \tag{28}$$

$$\left[\frac{C}{Pr_e}\Theta'\right]'+\frac{C}{Sc}\alpha_\delta z'\Theta'+\alpha_\delta zf\Theta'-\beta_{T_e}\alpha_\delta zf'\Theta+\epsilon_{el}\phi_{el}\alpha_\delta z\left[\frac{\theta}{\tau}-\Theta\right]$$
$$-\alpha_\delta[\epsilon_{fe}\phi_{fe}(1-\alpha_\delta z)z-\epsilon_{re}\phi_{re}z^3]\left[\frac{2}{5}\frac{T_I}{T_{e\delta}}+\Theta\right]-\alpha_\delta\Theta[\epsilon_{fa}\phi_{fa}(1-\alpha_\delta z)^2-\epsilon_{ra}\phi_{ra}(1-\alpha_\delta z)z^2]$$
$$=2\xi\alpha_\delta z\left[f'\frac{\partial\Theta}{\partial\xi}-\frac{\partial f}{\partial\xi}\Theta'\right], \tag{29}$$

where a prime denotes $\partial/\partial\eta$ and the following definitions are used:

$$f=\int_0^\eta\frac{u}{u_\delta}d\eta,\quad f'=\frac{u}{u_\delta},\quad z=\frac{\alpha}{\alpha_\delta},\quad\theta=\frac{T_a}{T_{a\delta}},\quad\Theta=\frac{T_e}{T_{e\delta}},\quad C=\frac{\rho\mu}{\rho_\delta\mu_\delta},$$
$$Sc=\frac{\mu}{\rho D_a},\quad Pr=\frac{\mu C_p}{\bar\lambda},\quad Pr_e=\frac{\mu C_p}{\lambda_e},\quad\beta_f=\frac{2\xi}{u_\delta}\frac{du_\delta}{d\xi},\quad\beta_z=\frac{2\xi}{\alpha_\delta}\frac{d\alpha_\delta}{d\xi},$$
$$\beta_{T_a}=\frac{2\xi}{T_{a\delta}}\frac{dT_{a\delta}}{d\xi},\quad\beta_{T_e}=\frac{2\xi}{T_{e\delta}}\frac{dT_{e\delta}}{d\xi},\quad\bar\lambda=\lambda_a+\lambda_i.$$

The quantity ρ_δ/ρ which appears in the transformed basic equations (26)–(29) is written as

$$\frac{\rho_\delta}{\rho}=\frac{\theta}{1+\alpha_\delta\tau}+\frac{\alpha_\delta\tau}{1+\alpha_\delta\tau}z\Theta. \tag{30}$$

It is seen that the boundary-layer equations for ionizing gases are strongly coupled dynamic and thermodynamic nonlinear partial differential equations. It should be noted that it is not feasible to apply the coupling method suggested by Tambour & Gal-Or (1977) to actual flows of the type considered here in view of the non-dimensional character of their analysis, which obscures the physical structure of the boundary layer.

Boundary and initial conditions

The boundary conditions for (1)–(5) are

$$\left.\begin{aligned}&u=0\ \text{(or } u_w \text{ for the shock-tube side-wall case)},\quad v=0,\quad T_a=T_w\quad\text{at}\quad y=0,\\&u=u_\delta,\quad\alpha=\alpha_\delta,\quad T_a=T_{a\delta},\quad T_e=T_{e\delta}\quad\text{as}\quad y\to\infty,\end{aligned}\right\} \tag{31}$$

where the wall values u_w and T_w are usually given. The other values u_δ, α_δ, $T_{a\delta}$ and $T_{e\delta}$ are determined from the inviscid flow region.

For the transformed equations (26)–(29) the boundary conditions (31) become

$$\left.\begin{aligned} f = 0, \quad f' = 0, \quad \theta = T_w/T_{a\delta} \qquad & \text{at} \quad \eta = 0, \\ f' = 1, \quad z = 1, \quad \theta = 1, \quad \Theta = 1 \quad & \text{as} \quad \eta \to \infty. \end{aligned}\right\} \tag{32}$$

The other boundary values required are z'_w and Θ'_w (or z_w and Θ_w), which are usually determined from the electric-sheath model:

$$z'_w = Sc_w \frac{(2\xi)^{\frac{1}{2}}}{\mu_w} \frac{V_{i\delta}}{u_\delta} z_w \Theta_w^{\frac{1}{2}}, \tag{33}$$

$$\Theta'_w = \frac{2}{5}\left(\frac{Pr_e}{Sc}\right)_w \left[-\tfrac{1}{2}\Theta_w + \frac{e\Delta\phi}{k_B T_{e\delta}}\right] \alpha_\delta z'_w, \tag{34}$$

where the subscript w denotes the wall value and

$$V_{i\delta} = (k_B T_{e\delta}/m_a)^{\frac{1}{2}},$$
$$e\Delta\phi/k_B T_{e\delta} = \ln (m_a/2\pi m_e)^{\frac{1}{2}} \Theta_w.$$

This model, based on continuity at the sheath edge, has been widely used by many authors. However, Mansfeld (1976), in considering the shock-tube thermal end-wall boundary layer, has mentioned that the artificial boundary conditions used for the two-temperature frozen model lead to values of n_e near the wall which seem to be in much better agreement with experimental results than the values obtained from consideration of an electric sheath. He concluded that the validity of the boundary condition for z and Θ at the wall derived from the present incomplete description of the sheath is still unknown.

For a cool-wall case, Takano & Akamatsu (1975) have shown that

$$z_w = O(10^{-2})/Re^{\frac{1}{2}}, \quad \Theta'_w = O(10^{-4}), \tag{35}$$

where Re is the Reynolds number. We also note that Nishida & Matsuoka (1971) have shown that the slope of the electron temperature at the wall is almost equal to zero. Mansfeld (1976) obtained similar results.

The initial conditions are required when using a finite-difference method. At the start of the boundary layer, $\xi = 0$ and the partial differential equations reduce to the following ordinary differential equations:

$$(Cf'')' + ff'' = 0, \tag{36}$$

$$\left(\frac{C}{Sc} z'\right)' + fz' = 0, \tag{37}$$

$$\left(\frac{C}{Pr} \theta'\right)' + f\theta' + \frac{u_\delta^2}{C_p T_{a\delta}} Cf''^2 = 0, \tag{38}$$

$$\left(\frac{C}{Pr_e} \Theta'\right)' + \frac{C}{Sc} \alpha_\delta z' \Theta' + \alpha_\delta z f \Theta' = 0. \tag{39}$$

Equations (36)–(39) with the two-point boundary conditions at the wall and at the boundary-layer edge can be solved using either a 'shooting technique' with a Newton–Raphson method or a finite-difference scheme. The former method was used in the present analysis.

Compatibility conditions and solutions for inviscid region

The parameters β appearing in (26)–(29) should be obtained from the compatibility conditions. At the edge of the boundary layer, the following boundary conditions must be satisfied as $\eta \to \infty$:

$$f'' = 0, \quad z' = 0, \quad \theta' = 0, \quad \Theta' = 0. \tag{40}$$

From these boundary conditions, the compatibility conditions at $\eta \to \infty$ can be obtained from (26)–(29) as

$$\beta_f = -\frac{2\xi}{\rho_\delta u_\delta^2}\frac{dp_\delta}{d\xi}, \tag{41}$$

$$\beta_z = \epsilon_{fa} - \epsilon_{ra} + \epsilon_{fe} - \epsilon_{re}, \tag{42}$$

$$\beta_{T_a} = -\beta_f \frac{u_\delta^2}{C_p T_{a\delta}} - \epsilon_{el}\alpha_\delta(1-\tau) - \epsilon_R - \frac{2}{5}\frac{T_I}{T_{a\delta}}\alpha_\delta(\epsilon_{fa} - \epsilon_{ra}), \tag{43}$$

$$\beta_{T_e} = \epsilon_{el}\left(\frac{1}{\tau} - 1\right) - (\epsilon_{fe} - \epsilon_{re})\left(\frac{2}{5}\frac{T_I}{T_{e\delta}} + 1\right) - \epsilon_{fa} + \epsilon_{ra}. \tag{44}$$

These conditions must be satisfied in the calculations in order to avoid a discontinuity in the gradients of the dependent variables at the edge of the boundary layer. The quantity $dp_\delta/d\xi$ appearing in (41) should be known from experiment or theory.

A local similarity method was applied by Brown & Mitchner (1971) to predict the electron-temperature and electron-number-density profiles of a flat-plate plasma boundary layer. They predicted that the electron temperature at the edge of boundary layer is smaller than the atom temperature and attributed this to the radiation-energy loss. However, it is clear that the compatibility conditions described above were not applied in their calculations. The electron temperature at the edge of boundary layer must be calculated from the equations for the inviscid flow and not from the boundary-layer equations. In the calculation of Brown & Mitchner, in order to satisfy the boundary conditions (40) at the edge of the boundary layer, the values of the degree of ionization and the electron temperature at the edge were adjusted.

The solutions for u_δ, $T_{a\delta}$, $T_{e\delta}$, α_δ and p_δ must be obtained from the equations for the inviscid region. The quasi-one-dimensional equations for inviscid flow are obtained from (1)–(5) by setting $\partial/\partial y = 0$:

$$d(\rho u)/dx = 0, \tag{45}$$

$$\rho u\, du/dx + dp/dx = 0, \tag{46}$$

$$\rho u\, dH/dx = -Q_R, \quad \rho u\, d\alpha/dx = m_a \dot{n}_e, \tag{47), (48}$$

$$\rho u\, d(\alpha C_p T_e)/dx - u\, dp_e/dx = Q_{el} + Q_{inel}. \tag{49}$$

Equations (45)–(49) have been solved by Glass & Liu (1978) for the shock-wave structure of ionizing argon and by Glass, Liu & Tang (1977) for krypton shock-wave structure. The inviscid flow generated by a shock wave can be separated into two zones: (i) an ionization-relaxation zone; (ii) a radiative-cooling zone. In the relaxation zone elastic and inelastic collisions are important while in the radiative-cooling zone

the radiation-energy loss is significant. Equations (45)–(49) provide a unified treatment applicable to both zones. However, from our numerical experience in solving for the shock-wave structure, a complete solution for the radiative-cooling region requires a small step size to be stable. As the plasma is nearly in equilibrium, values for u_δ, $T_{a\delta}$, $T_{e\delta}$, α_δ and p_δ in the cooling region can also be obtained approximately by solving only (45)–(47) together with the Saha equation. Whitten (1977) has shown that the results obtained from a radiant-equilibrium model are within 2 % of those obtained from the present non-equilibrium model.

3. Finite-difference method

An excellent review of the finite-difference method of solution of the boundary-layer equations was given by Blottner (1970). The nonlinear partial differential equations (26)–(29) with the boundary conditions of mixed Neumann and Dirichlet type are solved numerically by an implicit six-point finite-difference scheme. The equations are first linearized in a form suitable for an iteration scheme. Blottner (1970) stated that the order of solution of the equations is important. The momentum equation is solved first and the species equation must be solved before the atom-temperature equation. The linearized equations may be written in the common form

$$x_1^{(i)} W_{\eta\eta}^{(i)} + x_2^{(i)} W_\eta^{(i)} + x_3^{(i)} W^{(i)} = x_4^{(i)} W_\xi^{(i)} + x_5^{(i)}, \tag{50}$$

where $W^{(1)} = F$, $W^{(2)} = z$, $W^{(3)} = \theta$, $W^{(4)} = \Theta$ and $F = \partial f/\partial\eta$ or

$$f = \int_0^\eta F\, d\eta.$$

The expressions $x_j^{(i)}$ $(i = 1, \ldots, 4)$ for the momentum, species, atom-temperature and electron-temperature equations are listed in the appendix.

These linearized equations are of second order and are solved in order for the unknowns F, z, θ and Θ. The derivatives and the integral in the η direction are then expressed by three-point-difference formulae. The derivatives in the ξ direction are approximated by a backward-difference scheme. Let i and j be the indices of the η, ξ co-ordinates for the difference net at the point considered. Any function W is written in terms of the values at two adjacent points in the ξ direction as

$$W = \lambda W(i, j+1) + (1-\lambda)\, W(i,j), \tag{51}$$

where λ is a weighting factor which can be suitably adjusted for improving the convergence of the iteration scheme. The explicit method given by $\lambda = 0$ and $\lambda = \frac{1}{2}$ is the Crank–Nicolson method, while $\lambda = 1$ gives the implicit method.

In this formulation either equal intervals or unequal intervals in the η direction can be used. The interval in η direction is increased in a geometric progression as

$$\Delta\eta_{i+1}/\Delta\eta_i = k, \tag{52}$$

where k is a constant which is set at a value slightly greater than unity.

The following derivatives are introduced:

$$W_\eta = \frac{\lambda}{(1+k)\,k^i}\frac{1}{\Delta\eta_1}[W(i+1,j+1)+(k^2-1)\,W(i,j+1)-k^2W(i-1,j+1)]$$
$$+\frac{1-\lambda}{(1+k)\,k^i}\frac{1}{\Delta\eta_1}[W(i+1,j)+(k^2-1)\,W(i,j)-k^2W(i-1,j)], \tag{53}$$

$$W_{\eta\eta} = \frac{2\lambda}{(1+k)\,k^{2i-1}}\frac{1}{\Delta\eta_1^2}[W(i+1,j+1)-(1+k)\,W(i,j+1)+kW(i-1,j+1)]$$
$$+\frac{2(1-\lambda)}{(1+k)\,k^{2i-1}}\frac{1}{\Delta\eta_1^2}[W(i+1,j)-(1+k)\,W(i,j)+kW(i-1,j)], \tag{54}$$

$$W_\xi = \frac{1}{\Delta\xi}[W(i,j+1)-W(i,j)], \tag{55}$$

where $\Delta\eta_1$ is the first interval in the η direction and $\Delta\xi$ is the interval in the ξ direction.

The quantity ξ is evaluated at a point between two adjacent points as

$$\xi = \lambda\xi_{j+1}+(1-\lambda)\,\xi_j.$$

The values of f and f_ξ at a point $(i,j+1)$ are given by

$$f(i,j+1) = \sum_{l=1}^{i}\frac{k^{l-1}\Delta\eta_1}{6}\left[\left(\frac{2+3k}{1+k}\right)F(l-1,j+1)+\left(\frac{1+3k}{k}\right)F(l,j+1)\right.$$
$$\left.-\left(\frac{1}{k(1+k)}\right)F(l+1,j+1)\right], \tag{56}$$

$$f_\xi(i,j+1) = \sum_{l=1}^{i}\frac{k^{l-1}\Delta\eta_1}{6}\left[\left(\frac{2+3k}{1+k}\right)F_\xi(l-1,j+1)+\left(\frac{1+3k}{k}\right)F_\xi(l,j+1)\right.$$
$$\left.-\left(\frac{1}{k(1+k)}\right)F_\xi(l+1,j+1)\right], \tag{57}$$

where

$$F_\xi(l,j+1) = [F(l,j+1)-F(l,j)]/\Delta\xi.$$

Substituting (53)–(55) into (50) yields

$$A_i^{(t)}\,W^{(t)}(i-1,j+1)+B_i^{(t)}\,W^{(t)}(i,j+1)+C_i^{(t)}\,W^{(t)}(i+1,j+1) = D_i^{(t)}, \tag{58}$$

where $t = 1,\ldots,4$, $i = 1,\ldots,N$, $j = 1,\ldots,M$ and

$$A_i^{(t)} = a_i k x_1^{(t)} - c_i k^2 x_2^{(t)},$$
$$B_i^{(t)} = -a_i x_1^{(t)}(1+k)+c_i x_2^{(t)}(k^2-1)+\lambda x_3^{(t)} - x_4^{(t)}/\Delta\xi,$$
$$C_i^{(t)} = a_i x_1^{(t)}+c_i x_2^{(t)},$$
$$D_i^{(t)} = -b_i x_1^{(t)}\Delta^2 W - d_i x_2^{(t)}\Delta W-(1-\lambda)\,x_3^{(t)}\,W(i,j)-(x_4^{(t)}/\Delta\xi)\,W(i,j)+x_5^{(t)},$$
$$a_i = \frac{2\lambda}{(1+k)\,k^{2i-1}}\frac{1}{\Delta\eta_1^2},\quad b_i = \frac{2(1-\lambda)}{(1+k)\,k^{2i-1}}\frac{1}{\Delta\eta_1^2},$$
$$c_i = \frac{\lambda}{(1+k)\,k^i}\frac{1}{\Delta\eta_1},\quad d_i = \frac{1-\lambda}{(1+k)\,k^i}\frac{1}{\Delta\eta_1},$$
$$\Delta W = W(i+1,j)+(k^2-1)\,W(i,j)-k^2W(i-1,j),$$
$$\Delta^2 W = W(i+1,j)-(1+k)\,W(i,j)+kW(i-1,j).$$

The boundary conditions for the finite-difference equations are

$$\left.\begin{aligned} W^{(1)}(0,j+1) &= u_w/u_\delta \\ W^{(2)}(0,j+1) &= \begin{cases} 0 & \text{for} \quad z_w = 0 \\ W^{(2)}(1,j+1) - \lambda_1 \Delta\eta_1 & \text{for} \quad z'_w = \lambda_1 \end{cases} \\ W^{(3)}(0,j+1) &= T_w/T_{a\delta} \\ W^{(4)}(0,j+1) &= \begin{cases} W^{(4)}(1,j+1) - \lambda_2 \Delta\eta_1 & \text{for} \quad \Theta'_w = \lambda_2 \\ W^{(4)}(1,j+1) & \text{for} \quad \Theta'_w = 0 \end{cases} \end{aligned}\right\} \quad \text{at} \quad i = 0 \quad (\eta = 0),$$

$$\left.\begin{aligned} W^{(1)}(N,j+1) &= 1, \quad W^{(2)}(N,j+1) = 1 \\ W^{(3)}(N,j+1) &= 1, \quad W^{(4)}(N,j+1) = 1 \end{aligned}\right\} \quad \text{at} \quad i = N \quad (\eta \to \infty).$$

The computational scheme is an iterative one. First the momentum equation is solved with assumed distributions of species and atom and electron temperatures. Next the resulting velocity field is employed in the species equation. The resulting species field is then used in the atom-temperature and subsequently the electron-temperature equations. The new species and atom- and electron-temperature distributions are then used to replace the assumed ones and the process continues until the solutions converge to satisfy a preset criterion.

The criterion for convergence of the set of difference approximations to the differential equations was not investigated. However, Douglas & Jones (1963) stated that an implicit or Crank–Nicolson difference scheme is convergent for an equation of the same type as (50). The stability criteria for a system of nonlinear partial differential equations are difficult to determine. When the Crank–Nicolson scheme is applied, bounded oscillations in the ξ direction appear in the analysis. Crandall (1955) showed that, for a relatively large step size in the ξ direction, bounded oscillations are possible even for linear equations. Douglas (1956) also mentioned the possibility of oscillations in the solution when a Crank–Nicolson scheme is used with boundary conditions of the mixed type. These oscillations do not occur when a backward-implicit method is used. However, a smaller step size $\Delta\xi$ than the one used in the Crank–Nicolson scheme is needed for the backward-implicit scheme for the same accuracy. This results in more computation time. For the present case, the oscillations can be controlled by a suitable choice of the parameter λ.

In order to avoid a third-order derivative in the momentum equation, Blottner (1964, 1970) introduced a transformed normal velocity while retaining the continuity equation. However, in the present method, the stream function is introduced and the momentum equation is written as a second-order equation. The same implicit finite-difference method was used by Sells (1966) for a laminar compressible boundary layer and by Chan (1971) for a turbulent incompressible boundary layer.

The accuracy of the numerical solution has to be better than the accuracy of the different physical models. The models used for the description of the transport properties, chemical reactions and sheath theory have an accuracy of about $O(10^{-1})$. The accuracy of the experimental results is at best $O(10^{-2})$ Therefore it seems sufficient to obtain numerical results with an accuracy of $O(10^{-2})$. Once the accuracy of the problem has been determined, the upper bounds for $\Delta\xi$ and $\Delta\eta$ can be defined.

In the present analysis, unequal step sizes are used in order to decrease computation

time. The determination of error bounds for unequal step sizes is more complicated than for a regular network. However, the irregular discretization can be checked in the present program by comparing results with $k = 1$ and with $k \neq 1$. It was shown that the irregular discretization does not lead to larger inaccuracy or spoil the solution in the present program.

From our numerical experience of the present analysis, the Crank–Nicolson scheme yields a bound oscillation in the ξ direction. This oscillation does not damp out even for a very small step size $\Delta\xi$. Therefore decreasing the step size $\Delta\xi$ is not the best way to achieve higher accuracy. This oscillation can be checked by using different values of λ in the calculation starting from the optimum value 0·5 and increasing to the maximum value. The smallest value of λ which just eliminates the oscillation is the one to use. The best value of λ for the present analysis is 0·75, at which the oscillation damps out within two downstream steps and does not reappear. A more detailed description of the present theoretical analysis including the computer program is given by Liu (1978).

4. Comparison of theoretical and experimental results

Measurements of ionizing flat-plate boundary-layer flows have been reported (Tseng & Talbot 1971; Brown & Mitchener 1971; Bredfeldt *et al.* 1967) for low temperatures and low electron number densities. Under these conditions, the radiation-energy loss in the plasma is small and can be neglected for both the inviscid and the viscous flow region. Thus the conditions at the edge of the boundary layer can generally be calculated from a non-radiant model in which the free-stream flow quantities are constant and independent of time.

Figure 1 shows schematically the experimental generation of a flat-plate boundary-layer flow over an airfoil model with a sharp expansion corner in the UTIAS 10 × 18 cm Hypervelocity Shock Tube. Such a boundary layer can be regarded as developing in a steady flow if the shock wave is travelling at a constant velocity and the radiant-energy loss is small. However, for a flow induced by a stronger shock wave ($M_s \geqslant 13$), the radiation-energy loss becomes significant and the boundary layer develops in a somewhat unsteady (non-uniform) flow.

A typical analysis of the inviscid radiant flow behind a shock wave travelling at constant velocity is shown in figure 2. In this case, the shock wave is moving at a Mach number $M_s = 12{\cdot}8$ into quiescent argon at $p_0 = 5{\cdot}01$ torr and $T_0 = 297$ °K and has been shown at a location $x_s = 40$ cm past the leading edge of the flat plate. The gradients result from the radiation-energy loss. Clearly, as the non-stationary shock wave travels along the tube, the inviscid flow conditions above the plate change with time, introducing unsteadiness (non-uniformity). Along the flat plate, it is seen that u_δ and p_δ decrease as x increases from the leading edge (or as one moves closer to the shock front) while $T_{a\delta}$, $T_{e\delta}$ and α_δ all increase. However, the fact that the inviscid flow with respect to the plate is unsteady rather than steady with flow gradients is emphasized by a consideration of the overall momentum equation for the plasma. In a steady one-dimensional inviscid flow

$$\rho_\delta u_\delta du_\delta/dx = -dp_\delta/dx.$$

That is, the velocity gradient and pressure gradient should have opposite signs, which is not the case in this flow.

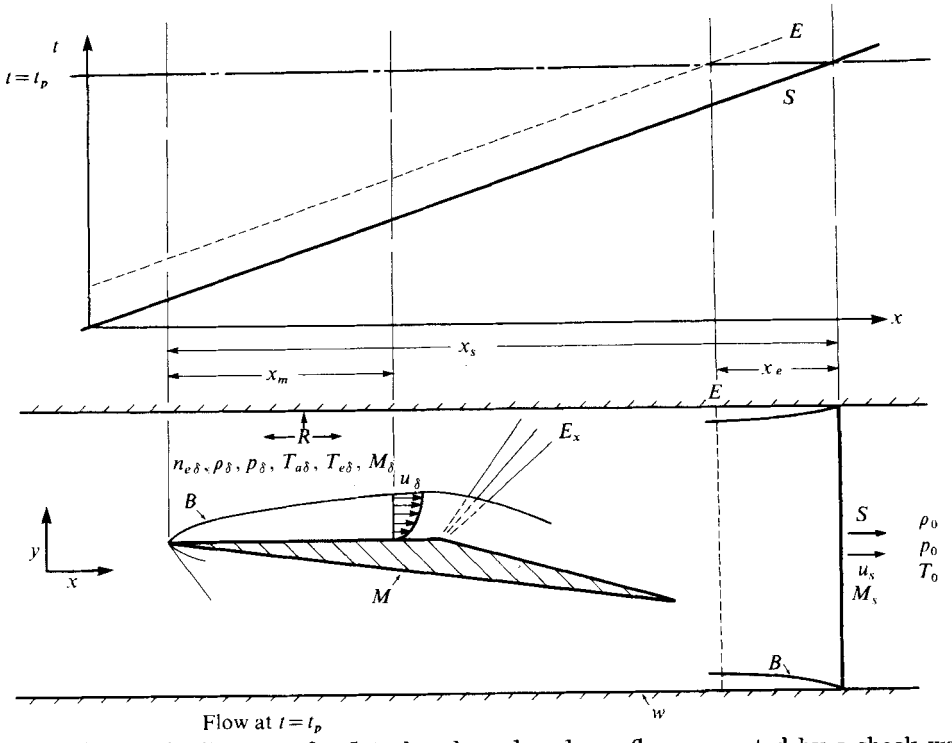

FIGURE 1. Schematic diagram of a flat-plate boundary-layer flow generated by a shock wave moving from left to right in a shock tube. S, translational shock wave; x_E, ionization-relaxation zone; E, electron cascade front; W, shock-tube walls; E_x, expansion wave; B, boundary layer; M, flat-plate model; R, radiative-cooling zone; other quantities as defined in the text.

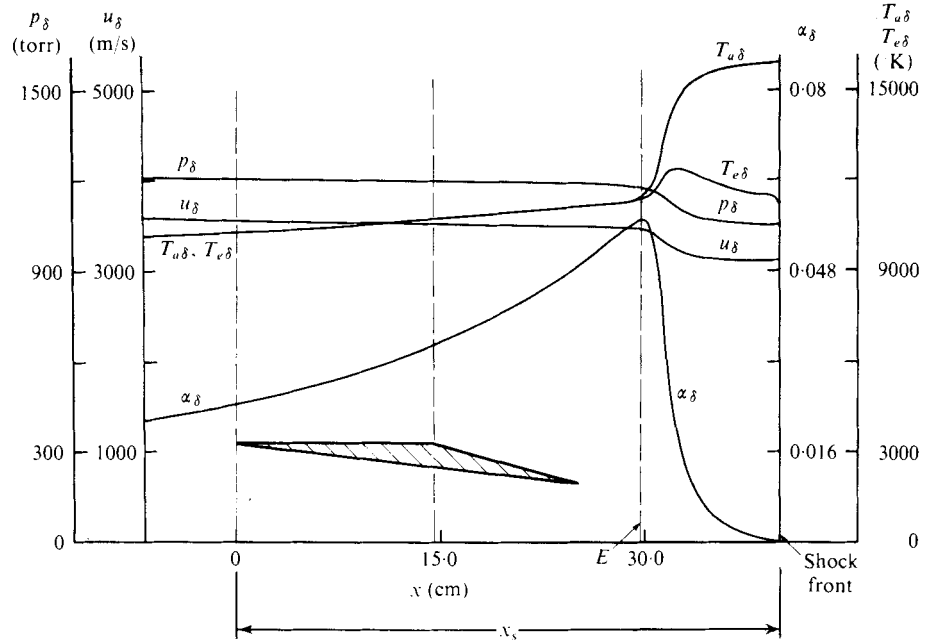

FIGURE 2. Variation of free-stream conditions at edge of boundary-layer flow with distance x from flat-plate leading edge for $M_s = 12{\cdot}8$, $p_0 = 5{\cdot}01$ torr and $T_0 = 297$ °K.

It can be seen, however, that the variations of u_δ, $T_{a\delta}$, $T_{e\delta}$ and p_δ are quite small, particularly as the distance x_s from the leading edge to the shock wave increases. Under these circumstances, it should be reasonable to regard the flat-plate boundary-layer flow as quasi-steady to a first-order approximation, so that the steady-flow analysis described in § 2 can be applied. It should be mentioned that the relative changes in α_δ are slightly larger, however, and the full extent of this effect on the assumption of quasi-steady flow is not known at present.

The experimental flow was examined using a Mach–Zehnder interferometer 23 cm in diameter to obtain interferograms simultaneously at two wavelengths of 6943 Å and 3471·5 Å. The electron number density and total-density changes (and hence the degree of ionization) were deduced from the interferograms (figure 3, plate 1). Additional details are given by Whitten (1977). Two cases were analysed experimentally and analytically. Figures 3 (*a*) and (*b*) show two interferograms at 6943 Å (the complementary interferograms at 3471·5 Å have been omitted here for brevity as they provide no further detail). Figure 3 (*a*) shows the shock wave for $M_s = 12{\cdot}8$, $p_0 = 5{\cdot}01$ torr and $T_0 = 297\,^\circ$K when it has just passed over the flat-plate portion of the airfoil and is diffracting around a 15° expansion corner. Readily seen are the translational shock front S, the relaxation zone SE, the electron cascade front E, where quasi-equilibrium ionization is achieved, and a small portion of the ensuing radiant flow. Figure 3 (*b*) shows the induced boundary-layer flow in a region 14 cm from the flat-plate leading edge, when the shock wave itself has reached a location 46 cm downstream from the leading edge. Figure 4 (*a*) (plate 2) shows an incident shock wave at $M_s = 16{\cdot}6$ in argon at an initial pressure $p_0 = 4{\cdot}81$ torr and initial temperature $T_0 = 296\,^\circ$K after it has passed over the flat plate and is diffracting around the 15° corner. The changes in shock structure and stability at this higher shock Mach number are apparent and are discussed in detail in Glass & Liu (1978). Figure 4 (*b*) (plate 2) again shows the induced boundary-layer flow 14 cm from the flat-plate leading edge, when the shock wave is 46 cm from the leading edge. Many details regarding the evaluation of such interferograms are given by Brimelow (1974) and Whitten (1977).

For comparison of boundary-layer profiles measured at a position x_m with analytical predictions, the inviscid flow conditions at x_m were assumed to prevail over the entire free-stream region (all x) in order to satisfy the assumption of steady flow in the analysis. The initial conditions for the shock wave and the free-stream quantities resulting from the radiant inviscid flow are listed in table 1.

In the finite-difference analysis, the best value of the weight parameter was found to be $\lambda = 0{\cdot}75$, at which the oscillations damped out during the first few steps. Case 2 of table 1 was run with $k = 1{\cdot}05$, $\Delta\eta_1 = 0{\cdot}05$ and $N = 46$ by using a step size Δx equal to 0·01 cm at $x = 0$ and increasing to 0·2 cm at $x = 14$ cm. At first the value 0·5 was used for the weighting parameter λ, and in all runs oscillations in f''_w and z'_w started at the first step downstream. The oscillations were bounded and tended to become small as x increased. In the next run $\lambda = 0{\cdot}75$ was used, and this time the oscillations damped out within two downstream steps and did not reappear. Therefore the Crank–Nicolson scheme ($\lambda = 0{\cdot}5$) was abandoned and $\lambda = 0{\cdot}75$ was used in the analysis.

For the case $M_s = 16{\cdot}6$ and $p_0 = 4{\cdot}81$ torr, the initial flow profiles (at $x = 0$) are shown in figure 5. The non-dimensional electron-temperature profile Θ is unity for all η, as a result of the electric-sheath condition $\Theta' = 0$ at $x = 0$. The atom-temperature profile θ increases from 0·029 at $\eta = 0$ to 1 at $\eta = 1{\cdot}95$, reaches a maximum value 1·04

Case ...	1	2
M_s	16·6	12·8
p_0 (torr)	4·81	5·01
T_0, T_w (°K)	296	297
u_δ (cm/s)	$4{\cdot}86 \times 10^5$	$3{\cdot}53 \times 10^5$
p_δ (torr)	2025	1200
$T_{a\delta}$ (°K)	$1{\cdot}049 \times 10^4$	$1{\cdot}065 \times 10^4$
α_δ	0·021	0·031
$n_{e\delta}$ (cm^{-3})	$3{\cdot}75 \times 10^{16}$	$3{\cdot}27 \times 10^{16}$
M_δ	2·9	2·1
a_δ (cm/s)	$1{\cdot}681 \times 10^5$	$1{\cdot}676 \times 10^5$
x_m (cm)	14	14
x_s (cm)	46	46
x_E (cm)	1·7	10·4

TABLE 1. Initial conditions and free-stream conditions for flat-plate boundary-layer flows.

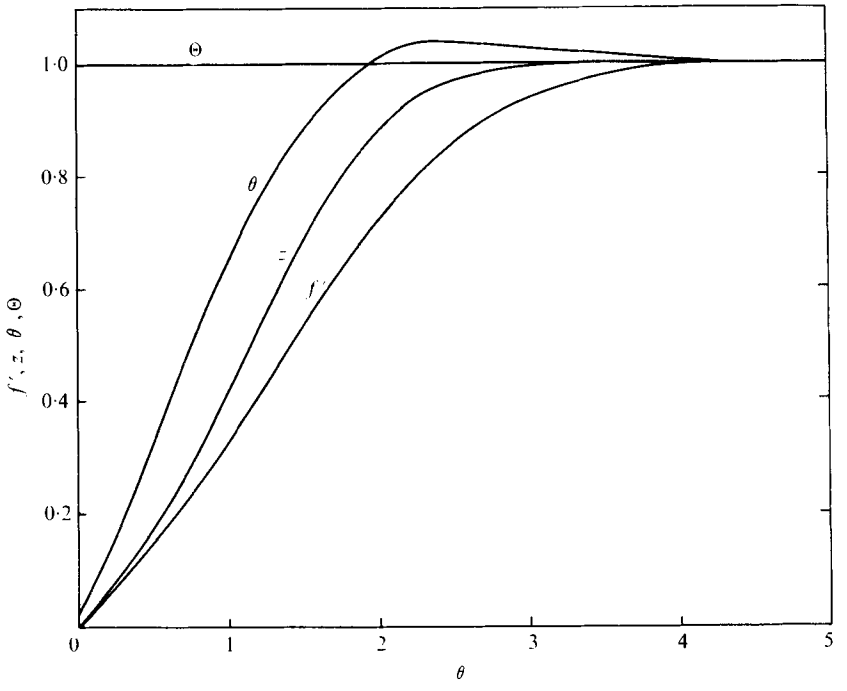

FIGURE 5. Initial profiles at $x = 0$ of the normalized velocity f', the degree of ionization z, the atom temperature θ and the electron temperature Θ *vs.* η for $M_s = 16{\cdot}6$, $p_0 = 4{\cdot}81$ torr and $T_0 = 296$ °K (case 1).

at $\eta = 2{\cdot}4$ and then approaches unity at $\eta = 4{\cdot}25$. The normalized velocity profile f' increases from zero at $\eta = 0$ to 1 at $\eta = 4{\cdot}5$, while the normalized degree of ionization z increases from 0 at $\eta = 0$ to 1 at $\eta = 3{\cdot}5$.

The variations of the transport properties Pr, Sc, C and Pr_e with η at $x = 0$ are shown in figure 6. The Prandtl number Pr for the heavy particles is constant ($Pr = 0{\cdot}667$) from its definition in this analysis. The ratio C of the density–viscosity products decreases from 2·8 at $\eta = 0$ to 1 at $\eta = 2{\cdot}23$. The Schmidt number Sc increases

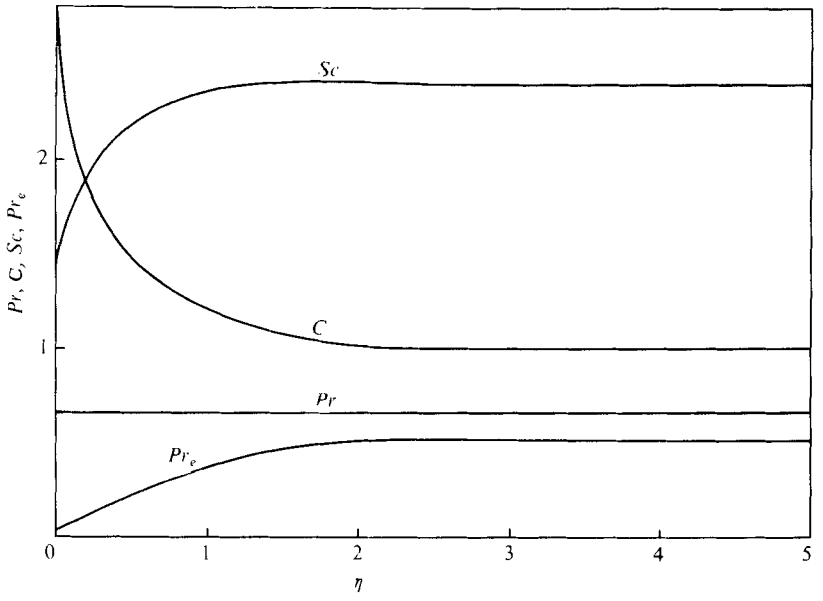

FIGURE 6. Variation of the heavy-particle Prandtl number Pr, the ratio C of density–viscosity products, the Schmidt number Sc and the electron Prandtl number Pr_e with η at $x = 0$ for $M_s = 16{\cdot}6$, $p_0 = 4{\cdot}81$ torr and $T_0 = 296$ °K (case 1).

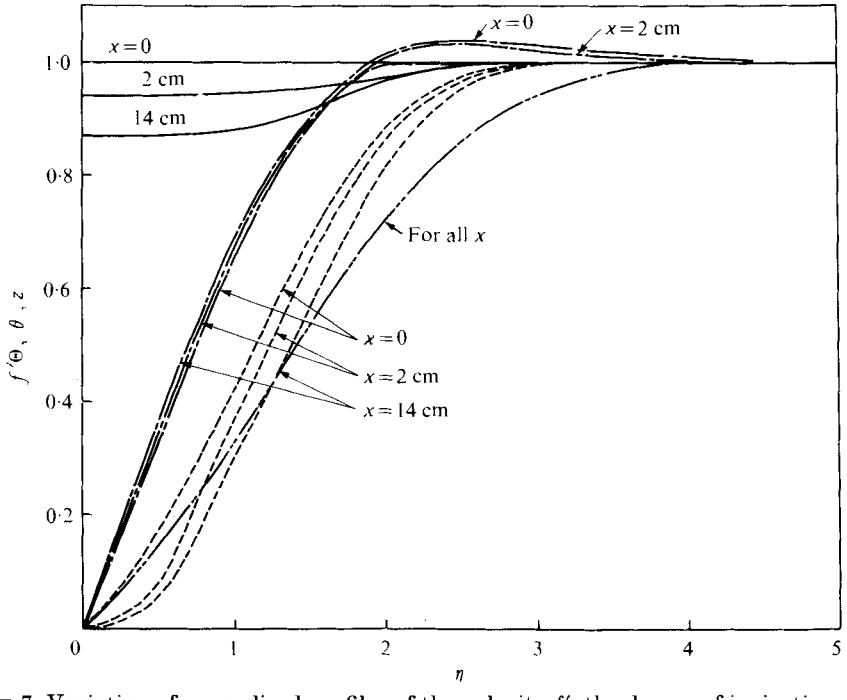

FIGURE 7. Variation of normalized profiles of the velocity f', the degree of ionization z, the atom temperature θ and the electron temperature Θ with the distance x from the leading edge for $M_s = 16{\cdot}6$, $p_0 = 4{\cdot}81$ torr and $T_0 = 296$ °K (case 1). ——·——, f'; ——, Θ; — — —, θ; – – – –, z.

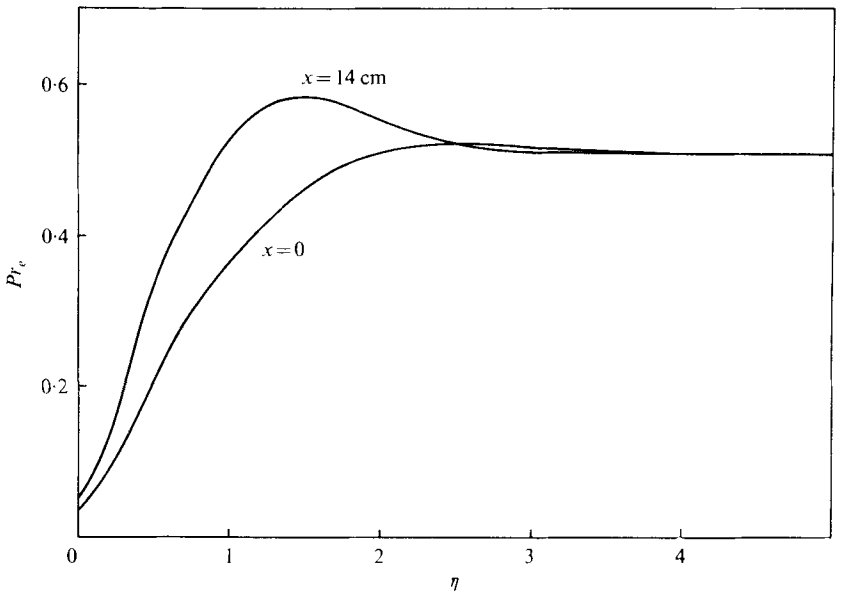

FIGURE 8. Variation of electron Prandtl number Pr_e with η at $x = 0$ and $x = 14$ cm for $M_s = 16{\cdot}6$, $p_0 = 4{\cdot}81$ torr and $T_0 = 296$ °K (case 1).

from 1·5 at $\eta = 0$ to 2·42 at $\eta = 1{\cdot}4$ then decreases to the free-stream value 2·39 at $\eta = 3{\cdot}12$. Similarly, Pr_e increases from 0·035 at $\eta = 0$ to 0·52 at $\eta = 2{\cdot}4$ then decreases to the free-stream value 0·507 at $\eta = 4{\cdot}79$. These parameters are functions of n_a, n_e, T_a, T_e and p_δ and their variations with η have some effect on the boundary-layer structure. The effect of Pr_e on the electron-temperature profile is more significant than that of C on the velocity profile and that of Pr on the atom-temperature profile. The total Prandtl number $\overline{Pr}$ of the plasma can be obtained from the equation

$$\overline{Pr}^{-1} = Pr^{-1} - Pr_e^{-1}.$$

The variations of the flow profiles with distance x are shown in figure 7. The velocity profile f' is almost independent of x. The variation of the atom-temperature ratio θ with x is also small. Therefore the momentum and atom-temperature equations can be obtained approximately from a similarity assumption. However, significant variations of the degree-of-ionization ratio z and electron-temperature ratio Θ with x do occur, as shown, and errors will result from a similarity assumption. The degree of ionization α and the electron temperature T_e decrease as x increases at a constant η. At $\eta = 0$, Θ_w decreases from 1 at $x = 0$ to 0·87 at $x = 14$ cm.

The variations of Pr_e with η for $x = 0$ and $x = 14$ cm are shown in figure 8. It is seen that, for $x = 14$ cm, Pr_e exceeds the free-stream value (0·507) from $\eta = 1$ to $\eta \sim 2{\cdot}5$.

In addition to the profiles of the various flow quantities across the boundary layer, parameters that characterize the skin friction, the heat transfer due to conduction and diffusion processes and the thickness of the boundary layer are important. The variations of the skin-friction parameter f''_w and the heat-transfer parameters θ'_w and z'_w for conduction and diffusion processes, respectively, with distance x are shown in figure 9. The values of f''_w are almost independent of x, while θ'_w increases at small x and approaches a constant value for large x. The quantity z'_w decreases significantly for

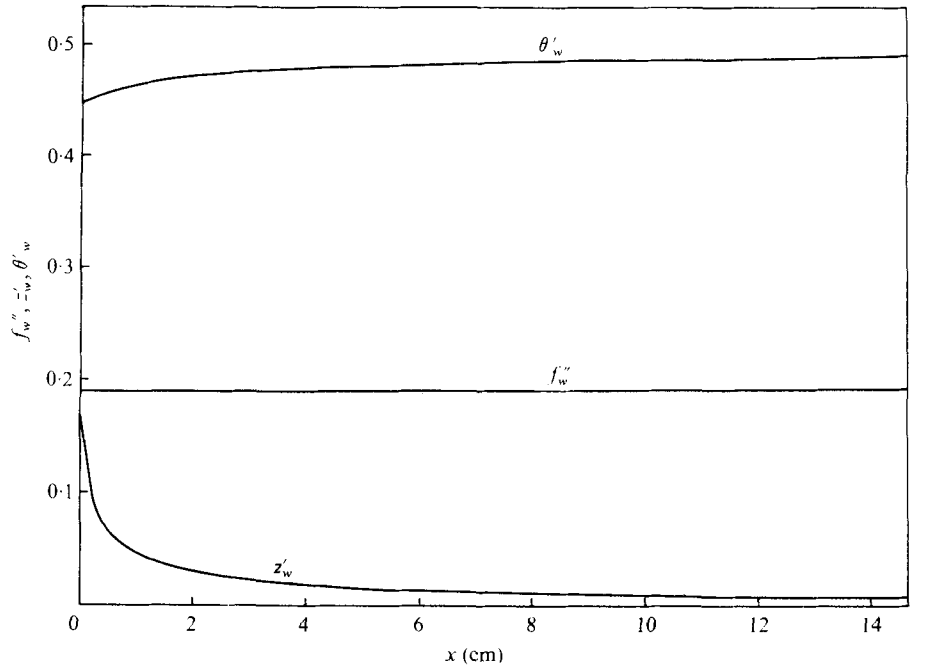

FIGURE 9. Variation of the skin-friction parameter (f''_w) and the heat-transfer parameters for conduction (θ'_w) and diffusion (z'_w) with x for $M_s = 16{\cdot}6$, $p_0 = 4{\cdot}81$ torr and $T_0 = 296$ °K (case 1).

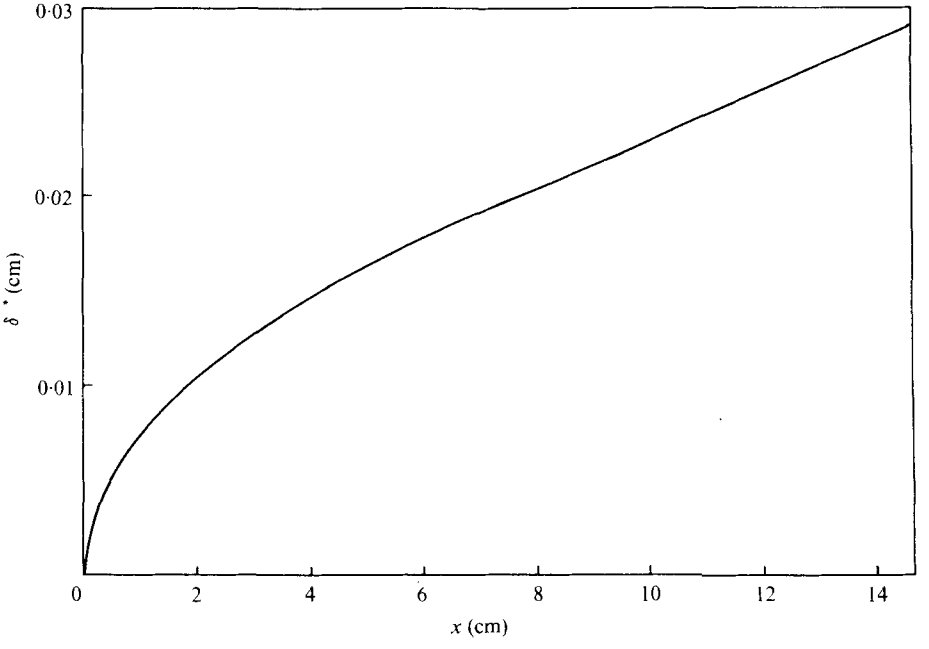

FIGURE 10. Variation of boundary-layer displacement thickness δ^* with x for $M_s = 16{\cdot}6$, $p_0 = 4{\cdot}81$ torr and $T_0 = 296$ °K (case 1).

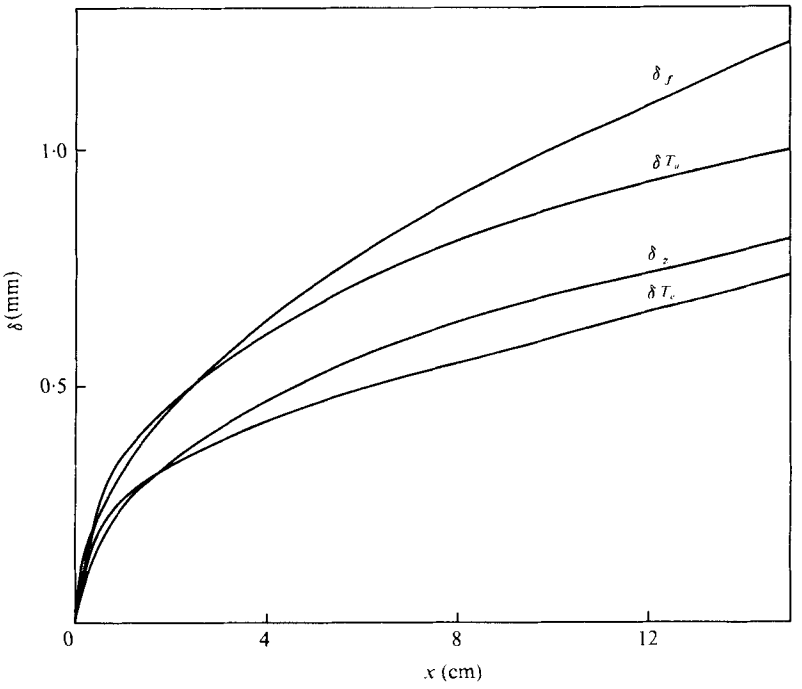

FIGURE 11. Variation of boundary-layer thicknesses of velocity (δ_f), degree of ionization (δ_z), atom temperature (δ_{Ta}) and electron temperature (δ_{Te}) with x for non-equilibrium flow for $M_s = 16{\cdot}6$, $p_0 = 4{\cdot}81$ torr and $T_0 = 296$ °K (case 1).

$x < 2$ cm and approaches a constant value for large x. The boundary-layer displacement thickness δ^* is plotted in figure 10 as a function of x. For x greater than 4 cm, δ^* increases almost linearly. The physical boundary-layer thicknesses for a flow-quantity ratio of 0·995 for the velocity (δ_f), the degree of ionization (δ_z), the atom temperature (δ_{T_a}) and the electron temperature (δ_{T_e}) are plotted in figure 11. It can be seen that the boundary-layer ($x > 3$ cm) thickness for velocity is greater than the other boundary-layer thicknesses for this case. The thickness δ_{T_e} of the electron thermal layer is less than the velocity thickness, which differs from the result found by Honma & Komuro (1976) for a side-wall boundary-layer flow. They showed that the thickness of the electron thermal layer is almost ten times the velocity or atom-temperature thicknesses.

The large variation in the chemical-reaction rates with temperature has an important effect on the boundary-layer structure for a large degree of ionization as shown in figure 12. The results for a frozen flow ($\dot{n}_e = 0$) are compared with those for a non-equilibrium flow at $x = 14$ cm and $M_s = 16{\cdot}6$. The profiles of the velocity f' and heavy-particle temperature θ hardly differ for the two cases. However the profiles of the electron temperature Θ, the degree of ionization z and the electron Prandtl number Pr_e are significantly affected by the chemical reactions. For a given η, the electron temperature Θ is lower for a frozen flow than for a non-equilibrium flow, while the reverse is true for the degree of ionization z.

Comparisons of analysis with experimental results (Whitten 1977) are shown in figures 13 and 14 for the plasma density and electron number density, respectively.

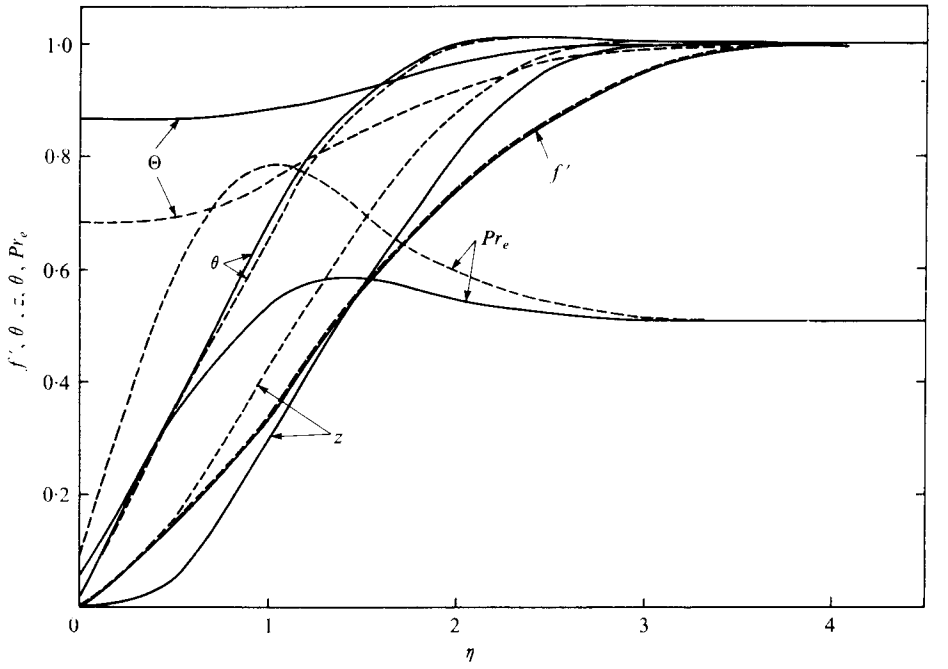

FIGURE 12. Normalized profiles of the velocity f', the atom temperature θ, the electron temperature Θ, the degree of ionization z and the electron Prandtl number Pr_e *vs.* η at $x = 14$ cm for $M_s = 16{\cdot}6$, $p_0 = 4{\cdot}81$ torr and $T_0 = 296$ °K (case 1). ——, non-equilibrium; – – –, frozen.

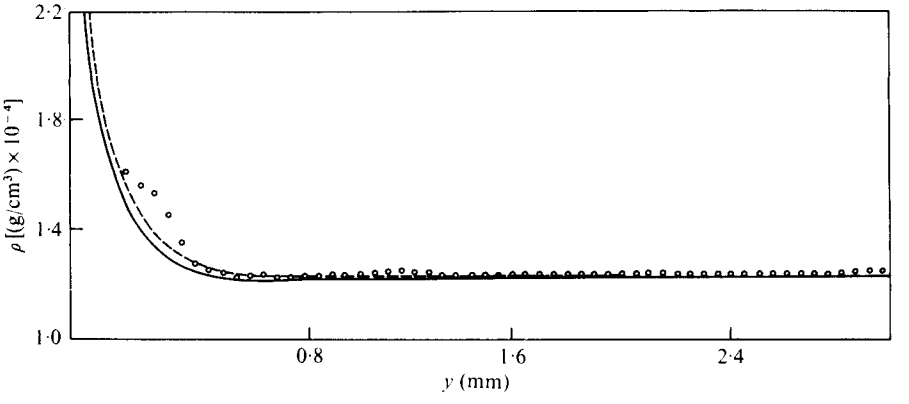

FIGURE 13. Comparison of analytical and experimental profiles of the plasma density ρ *vs.* the distance y across the boundary layer at $x = 14$ cm for $M_s = 16{\cdot}6$, $p_0 = 4{\cdot}81$ torr and $T_0 = 296$ °K (case 1). ——, non-equilibrium; – – –, frozen.

Better agreement is obtained between the measured plasma-density profile and the frozen-flow analysis. However, poor agreement is obtained between the measured electron-number density profile and either solution. The experimental data show a significant bump in the n_e profile which is not predicted by either the non-equilibrium or the frozen-flow analysis. A similar bump appears in the experimental data for the degree-of-ionization profile shown in figure 15, while there is no bump in the analytical result. This disagreement has not been resolved.

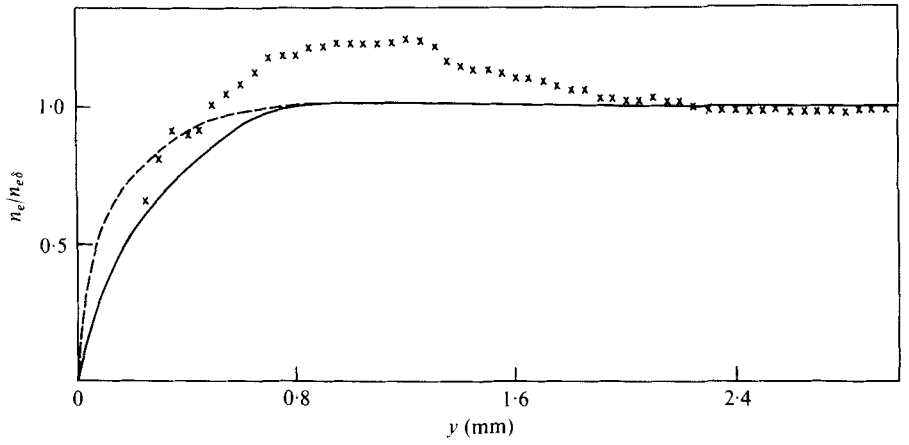

FIGURE 14. Comparison of analytical and experimental profiles of normalized electron number density $n_e/n_{e\delta}$ *vs.* y at $x = 14$ cm for $M_s = 16{\cdot}6$, $p_0 = 4{\cdot}81$ torr, $T_0 = 296$ °K (case 1) and $n_{e\delta} = 0{\cdot}372 \times 10^{17}$ cm^{-3}. ——, non-equilibrium; – – –, frozen.

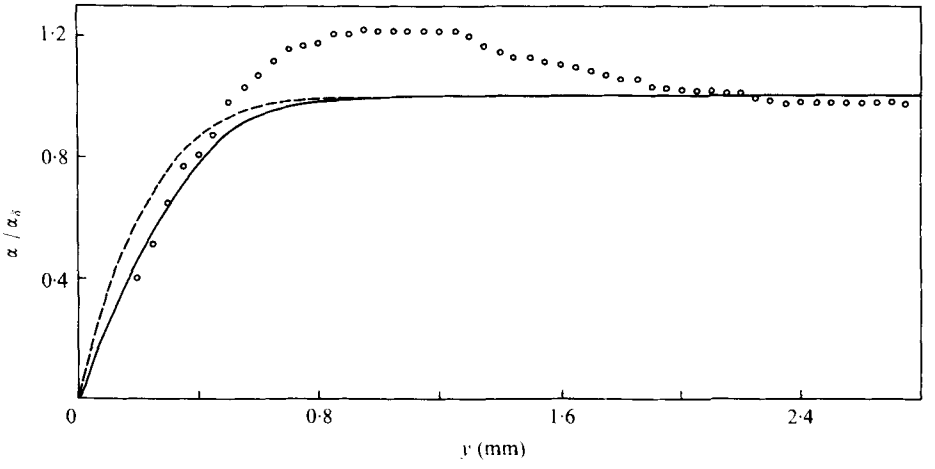

FIGURE 15. Comparison of analytical and experimental profiles of normalized degree of ionization α/α_δ *vs.* y at $x = 14$ cm for $M_s = 16{\cdot}6$, $p_0 = 4{\cdot}81$ torr, $T_0 = 296$ °K (case 1) and $\alpha_\delta = 0{\cdot}0203$. ——, non-equilibrium; – – –, frozen.

For the second case $M_s = 12{\cdot}8$, $p_0 = 5{\cdot}01$ torr and $T_0 = 297$ °K, the non-equilibrium and frozen-flow profiles at $x = 14$ cm are shown in figures 16 and 17, respectively. Here also significant differences exist for the degree-of-ionization and electron-temperature profiles. The analytical and experimental results for the plasma-density and electron-number-density profiles are compared in figures 18 and 19, respectively, while the corresponding degree-of-ionization profile is shown in figure 20. Unlike case 1, the experimental plasma-density data show better agreement with the non-equilibrium or the calculated equilibrium similarity-solution profiles, which are very close. The experimental results for n_e lie between the analytical non-equilibrium and frozen-flow profiles. The two-temperature frozen-flow solution predicts a larger bump than that obtained from the experiment, while no bump occurs in the non-equilibrium or

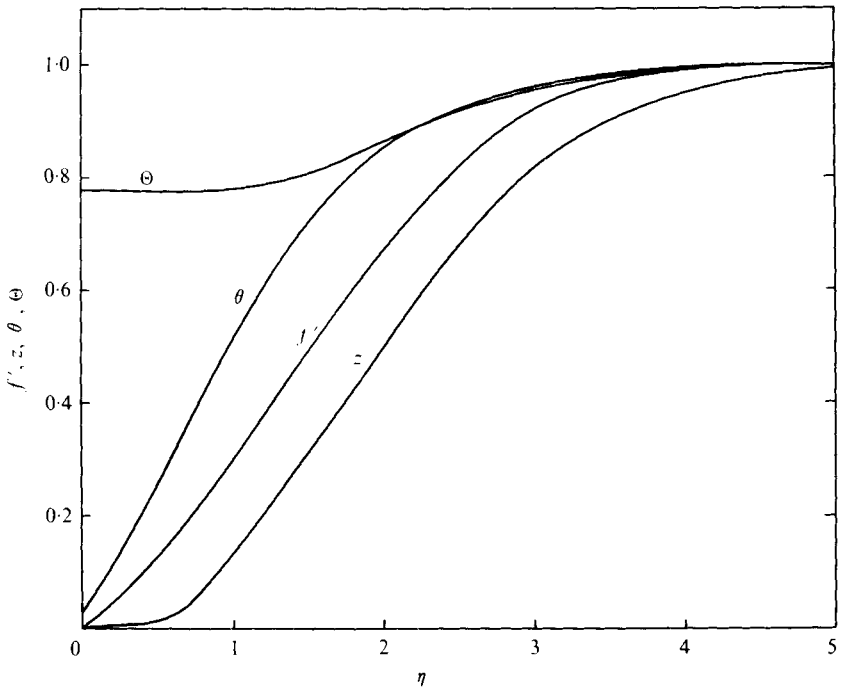

FIGURE 16. Non-equilibrium profiles of the normalized velocity f', degree of ionization z, atom temperature θ and electron temperature Θ as a function of η at $x = 14$ cm for $M_s = 12{\cdot}8$, $p_0 = 5{\cdot}01$ torr and $T_0 = 297$ °K (case 2).

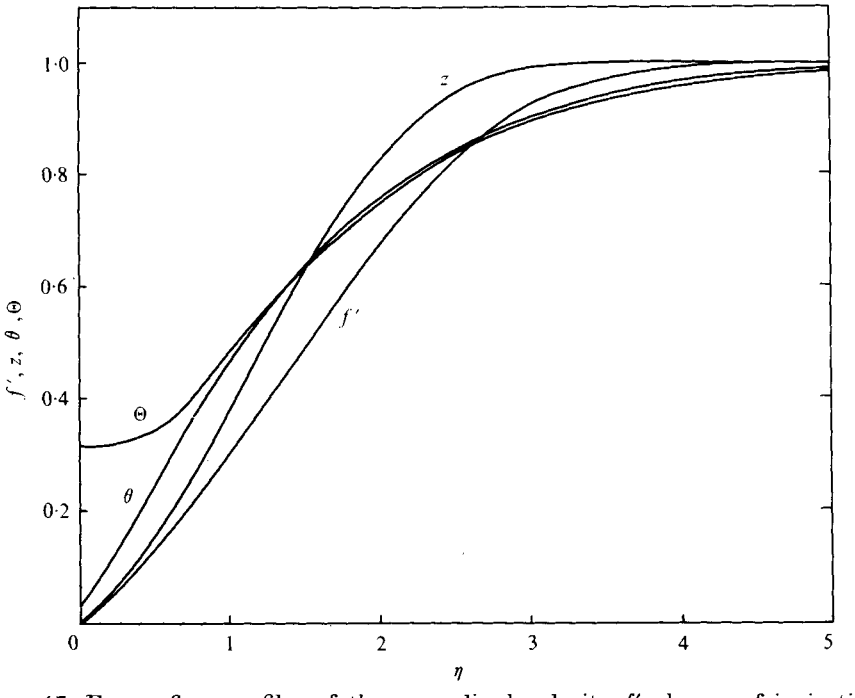

FIGURE 17. Frozen-flow profiles of the normalized velocity f', degree of ionization z, atom temperature θ and electron temperature Θ as a function of η at $x = 14$ cm for $M_s = 12{\cdot}8$, $p_0 = 5{\cdot}01$ torr and $T_0 = 297$ °K (case 2).

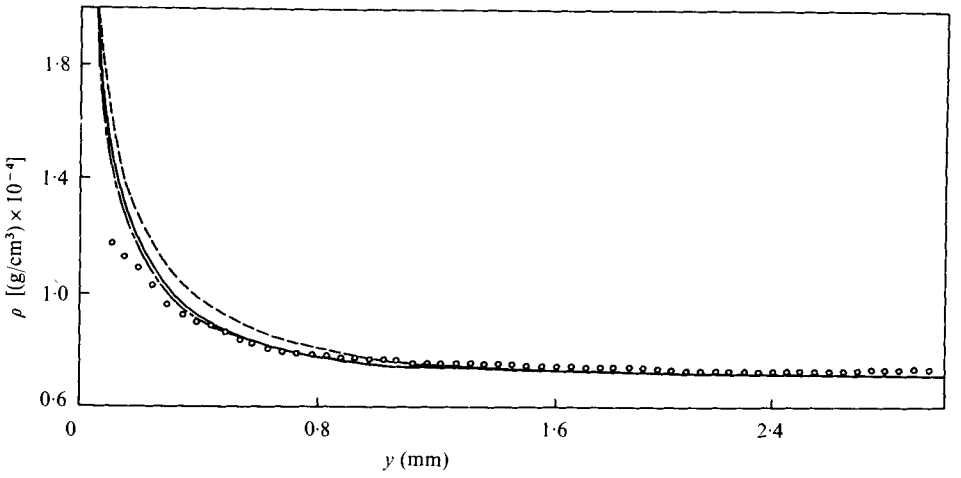

FIGURE 18. Comparison of analytical and experimental profiles of the plasma density ρ *vs.* y at $x = 14$ cm for $M_s = 12{\cdot}8$, $p_0 = 5{\cdot}01$ torr and $T_0 = 297$ °K (case 2). ——, non-equilibrium; – – –, frozen; —·—, equilibrium similarity solution.

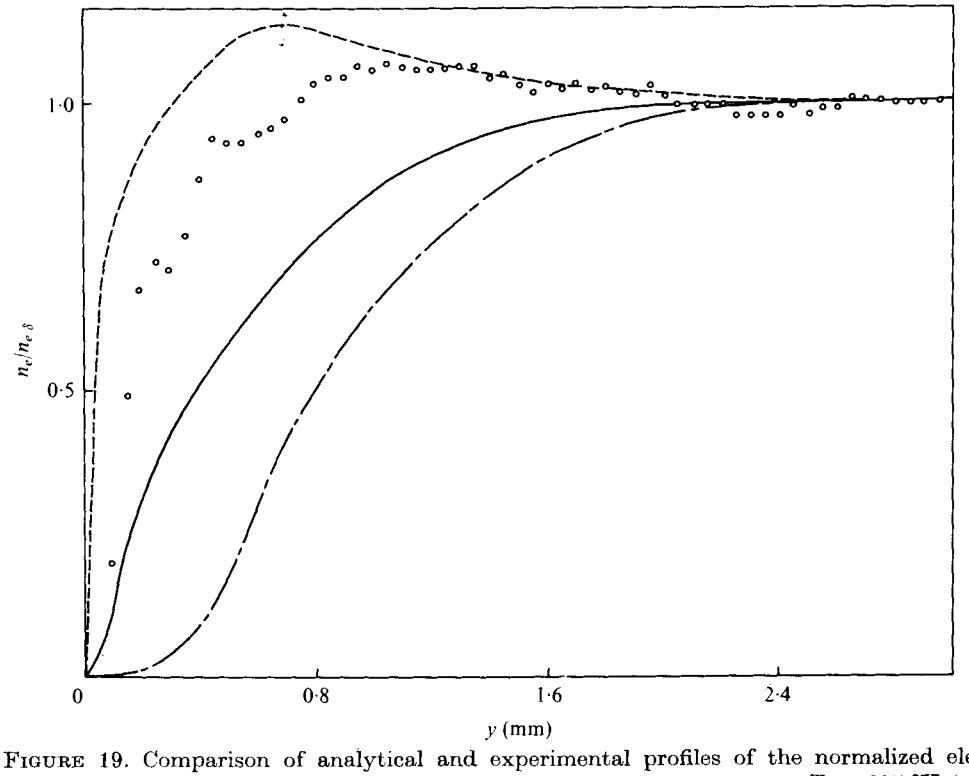

FIGURE 19. Comparison of analytical and experimental profiles of the normalized electron number density $n_e/n_{e\delta}$ *vs.* y at $x = 14$ cm for $M_s = 12{\cdot}8$, $p_0 = 5{\cdot}01$ torr, $T_0 = 297$ °K (case 2) and $n_{e\delta} = 3{\cdot}3 \times 10^{16}$ cm^{-3}. ——, non-equilibrium; – – –, frozen; —·—, equilibrium similarity solution.

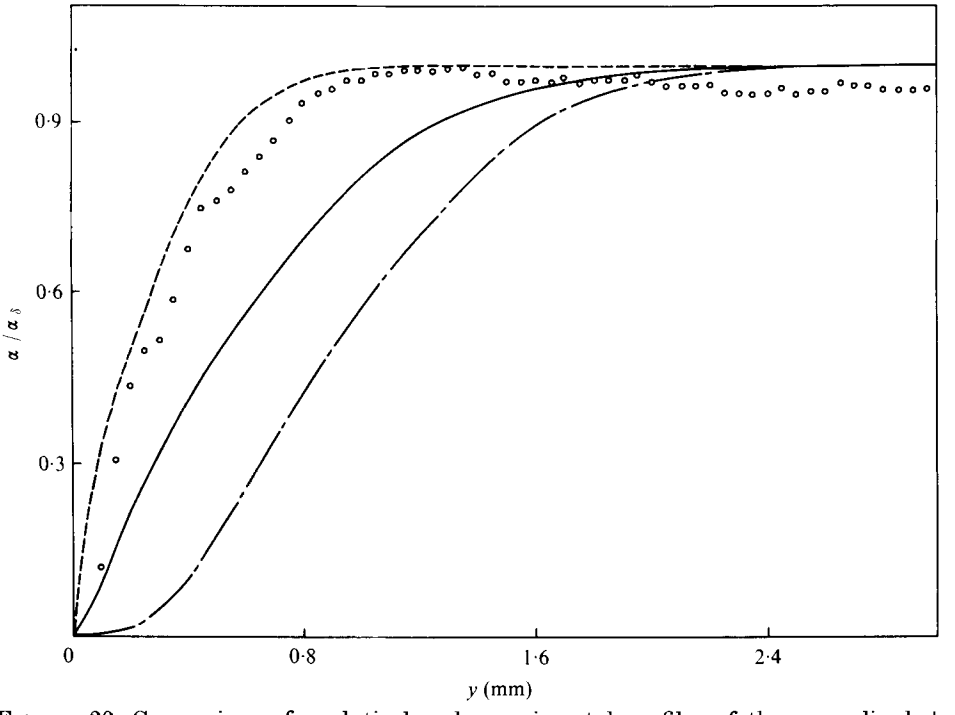

FIGURE 20. Comparison of analytical and experimental profiles of the normalized degree of ionization α/α_δ *vs.* y at $x = 14$ cm for $M_s = 12{\cdot}8$, $p_0 = 5{\cdot}01$ torr, $T_0 = 297$ °K (case 2) and $\alpha_\delta = 0{\cdot}031$. ——, non-equilibrium; – – –, frozen; ——·——, equilibrium similarity solution.

equilibrium profiles. The experimental data for the degree of ionization lie closer to the calculated frozen-flow profile than to the non-equilibrium profile.

The local-similarity solutions (Whitten 1977) based on thermal and chemical equilibrium are also plotted in figures 18–20 for case 2. It is seen that equilibrium will not occur in such boundary-layer flows. Of the three models used in the analyses for n_e and α, the equilibrium profiles provide the worst agreement with the experimental results. The n_e profile is the most sensitive indicator of the state of the boundary layer. The fact that the density data agree with the three models used in the analyses shows that density is not a sensitive parameter. Undoubtedly, measurements of electron and heavy-particle temperatures are desirable as they would be sensitive indicators of the state of the boundary layer.

The disagreement between theory and experiment for n_e (or α) may result from two sources.

(i) The boundary-layer flow is assumed to be quasi-steady while in the experiments it is unsteady owing to radiation losses (which were only partially accounted for) and the effects of the side-wall boundary layers (which were not taken into account at all and have effects similar to those of radiation). These effects will be more pronounced at higher shock Mach numbers, when the radiation-energy loss is significant. For example, the agreement between theory and experiment for $M_s = 16{\cdot}6$ is worse than that for $M_s = 12{\cdot}8$ for the n_e and α profiles. In order to assume that the boundary-layer flow was quasi-steady, the variation of the flow quantities at the edge of the boundary

layer with distance was neglected in the theory. This error might have a significant effect on the boundary-layer structure.

(ii) The assumptions made in the basic equations (such as $\rho_i V_i \approx -\rho D_a \partial\alpha/\partial y$ and $\mathbf{v} \cdot \nabla p_e \approx 0$), the uncertainty in the parameters used to describe the elastic and inelastic energy-transfer rates and the model used for the radiation-energy loss may all affect the entire boundary-layer structure. However, the agreement of analysis with experiment for the case $M_s = 12{\cdot}8$ is quite good and suggests that the assumptions made in the basic equations are reasonable. Furthermore, from the analyses of shock-wave structure (Glass & Liu 1978; Glass *et al.* 1977), the parameters used for the elastic and inelastic energy transfer and the radiation model are considered accurate within the limitations of present-day collision theory.

As noted earlier, some possible errors in the present analysis may result from neglecting the reabsorption of the radiation-energy loss in the free stream and the effects of the side-wall boundary layers on the free-stream flow. An exact solution to the set of simultaneous ordinary differential equations for the free-stream flow including reabsorption would be difficult since the reabsorption coefficient is a function of the complete structure of the radiation-cooling zone. The question would also arise as to whether the shock tube has a finite or an infinite optical depth. The Rosseland mean free path for argon under the free-stream conditions $M_s = 16{\cdot}6$, $p_0 = 4{\cdot}81$ torr and $T_0 = 296\,^{\circ}\mathrm{K}$ (case 1) is about 97 cm. Therefore the free-stream plasma is optically thin and the reabsorption energy should be small. For the present calculations it was necessary to consider the worst case when there is no reabsorption. The shock-tube side-wall boundary layer will have some effects on the free-stream conditions. In general, it would be desirable to study the present flat-plate boundary layer after the effects of the shock-tube side-wall boundary layers on the free stream had been determined. In the present analysis the free-stream conditions were obtained under the assumption that the flow was one-dimensional; the role of the growth of the side-wall boundary layer on the inviscid flow was not considered. Mirels (1966) has shown that the flow between the shock wave and contact surface in an actual shock tube is non-uniform owing to the wall boundary layer. Recently, Enomoto (1973) has studied the effects of the boundary-layer growth in shock tubes of various cross-sections on the shock-wave ionization-relaxation process in argon. He used Mirels' boundary-layer theory for a perfect gas to get some estimates and showed that consideration of the side-wall boundary layer effects shortened the ionization-relaxation time. The inclusion of reabsorption of radiation energy and side-wall boundary-layer effects will increase the degree of ionization in the free-stream. Neglecting these two effects in the analysis might alter the free-stream conditions. In order to study the effects of the free-stream conditions on the boundary-layer structure for the case $M_s = 16{\cdot}6$, when the theoretical and experimental boundary-layer thicknesses for n_e are 0·8 mm and 2 mm, respectively ($x = 14$ cm), three different free-stream values (at $t = 20\,\mu$s, $40\,\mu$s and $60\,\mu$s after the passage of the shock wave) were used for comparison. Even then, the theoretical boundary-layer thicknesses for n_e were between 0·8 mm and 1·2 mm and still differed from the experimental results. It was shown that the boundary-layer thickness for n_e increases as the degree of ionization in the free stream increases.

It is worth noting that the error due to neglecting the photo-ionization in the analysis may not be small. Near the wall, where the ionization due to electron–atom collisions is small compared with that in the free stream, photons resulting from

stimulated emission and radiation processes may have an opportunity to ionize atoms. The population of the photon flux should be known before any calculation on the photo-ionization rate can be done.

Finally, from a comparison of the theoretical results of Mansfeld (1976) and the experimental results of Kuiper (1968) for a thermal Rayleigh boundary layer, it was shown that the frozen models lead to values of n_e near the wall which seem to be in much better agreement than the values obtained from a non-equilibrium model. No bump in n_e occurred in either theory or experiment for a thermal Rayleigh boundary layer.

5. Conclusions

The complete set of partial differential equations for a laminar boundary layer in ionizing argon have been solved by a six-point implicit finite-difference scheme. The new features in the analysis are the inclusion of radiation-energy loss and the appropriate chemical reactions, the latter including the atom–atom reactions. Account was taken of the variation across the boundary layer of the transport properties based on the known elastic-scattering cross-sections for an argon plasma. The compatibility conditions and the electric-sheath model were described and incorporated into the analysis. The flat-plate boundary-layer flows were analysed and compared with interferometric data obtained using the UTIAS 10×18 cm Hypervelocity Shock Tube equipped with a Mach–Zehnder dual-wavelength interferometer of diameter 23 cm at shock Mach numbers $M_s = 12{\cdot}8$ and $16{\cdot}6$ and an initial argon pressure $p_0 \approx 5$ torr and temperature $T_0 \approx 297\,^{\circ}\mathrm{K}$.

The analysis is probably the most complete and detailed that has been undertaken to date. It clearly shows that the measured electron-number-density and degree-of-ionization profiles in the boundary layer for equilibrium, frozen and non-equilibrium flows are more sensitive than the measured complementary total-number-density profile for determining the actual state of the boundary layer, as might have been expected. Agreement between theory and experiment for the density profiles appears to be good to excellent as there is little difference between the three analytical profiles. However, agreement of experiment with analysis for the electron number density (or degree of ionization) is only fair. The experimental data lie between the analytical frozen and non-equilibrium profiles. The data show a bump in the n_e profiles at both $M_s = 16{\cdot}6$ and $M_s = 12{\cdot}8$, while theory can predict a bump only for the frozen case at $M_s = 12{\cdot}8$. The unsteadiness of the inviscid flow may have an important effect on the boundary-layer structure at high shock Mach numbers, when the radiation-energy loss is significant. In addition, the values of Pr_e may be inaccurate and as a consequence the experiments tend to show that the boundary-layer flows lie between a frozen and a non-equilibrium state. Measurements of electron and heavy-particle temperatures would have been very valuable to complement the present results. Our interferometric data must be considered as very reliable. The same techniques were employed to determine shock-structure profiles (see Glass & Liu 1978; Glass *et al.* 1977) and argon–argon and krypton–krypton atomic collision cross-sections, which agreed well with those obtained by other methods. Consequently, when improvements have been made in calculating ionizing flow-transport properties and full account can be taken of the flow non-uniformities caused by radiation and its reabsorption as well as those induced

by the side-wall boundary layers, it will still be possible to use the present interferometric data to test the validity of the improved analyses.

The financial assistance received from the National Research Council of Canada and the U.S. Air Force Office of Scientific Research under Grant AF-AFOSR 77-3303 is acknowledged with thanks.

Appendix. Expressions for the functions $x_j^{(i)}$

For $i = 1$ and $W^{(1)} = F$,

$$x_1 = C, \quad x_2 = C_\eta + f + 2\xi f_\xi, \quad x_3 = -\beta_f F, \quad x_4 = 2\xi F, \quad x_5 = -\beta_f(\rho_\delta/\rho),$$

For $i = 2$ and $W^{(2)} = z$,

$$x_1 = C/Sc, \quad x_2 = (C/Sc)_\eta + f + 2\xi f_\xi, \quad x_3 = -\beta_z F + \Phi, \quad x_4 = 2\xi F, \quad x_5 = -\epsilon_{fa}\phi_{fa}.$$

For $i = 3$ and $W^{(3)} = \theta$,

$$x_1 = C/Pr, \quad x_2 = (C/Pr)_\eta + f + 2\xi f_\xi,$$

$$x_3 = -BF - \epsilon_{el}\phi_{el}\alpha_\delta z, \quad x_4 = 2\xi F,$$

$$x_5 = -\frac{u_\delta^2}{C_p T_{a\delta}} CF_\eta^2 + \beta_f \frac{\alpha_\delta z}{1+\alpha_\delta \tau} z\Theta \frac{u_\delta^2}{C_p T_{a\delta}} F - \epsilon_{el}\phi_{el}\alpha_\delta z\tau\Theta + \epsilon_R \phi_R \left(\frac{\rho}{\rho_\delta}\right)$$
$$+ \frac{2}{5}\frac{T_I}{T_{a\delta}}\alpha_\delta[(1-\alpha_\delta z)^2 \epsilon_{fa}\phi_{fa} - z^2(1-\alpha_\delta z)\epsilon_{ra}\phi_{ra}].$$

For $i = 4$ and $W^{(4)} = \Theta$,

$$x_1 = C/Pr_e, \quad x_2 = (C/Pr_e)_\eta + (C/Sc)\alpha_\delta z_\eta + \alpha_\delta z f + 2\xi\alpha_\delta z f_\xi,$$

$$x_3 = -\beta_{T_e}\alpha_\delta zF - \epsilon_{el}\phi_{el}\alpha_\delta z - \alpha_\delta G - \alpha_\delta[\epsilon_{fa}\phi_{fa}(1-\alpha_\delta z)^2 - \epsilon_{ra}\phi_{ra}z^2(1-\alpha_\delta z)],$$

$$x_4 = 2\xi F\alpha_\delta z, \quad x_5 = -\epsilon_{el}\phi_{el}\alpha_\delta z\frac{\theta}{\tau} + \tfrac{2}{5}\alpha_\delta \frac{T_I}{T_{e\delta}} G.$$

Here

$$B = \beta_{T_a} + \frac{\beta_f}{1+\alpha_\delta\tau}\frac{u_\delta^2}{C_p T_{a\delta}},$$

$$\Phi = (\alpha_\delta^2 z - 2\alpha_\delta)\epsilon_{fa}\phi_{fa} - \epsilon_{ra}\phi_{ra}z(1-\alpha_\delta z) + \epsilon_{fe}\phi_{fe}(1-\alpha_\delta z) - \epsilon_{re}\phi_{re}z^2,$$

$$G = \epsilon_{fe}\phi_{fe}(1-\alpha_\delta z)z - \epsilon_{re}\phi_{re}z^3.$$

REFERENCES

AMDUR, I. & MASON, E. A. 1958 *Phys. Fluids* **1**, 370.

APPLETON, J. P. & BRAY, K. N. C. 1964 *J. Fluid Mech.* **20**, 659.

BACK, L. H. 1967 *Phys. Fluids* **10**, 807.

BLOTTNER, F. G. 1964 *A.I.A.A. J.* **2**, 1921.

BLOTTNER, F. G. 1970 *A.I.A.A. J.* **8**, 193.

BREDFELDT, H. R., SCHARFMAN, W. E., GUTHART, H. & MORITA, T. 1967 *A.I.A.A. J.* **5**, 91.

BRIMELOW, P. I. 1974 M.Sc. thesis, University of Toronto.

BROWN, R. T. & MITCHNER, M. 1971 *Phys. Fluids* **14**, 933.

BYRON, S., STABLER, R. C. & BORTZ, P. I. 1962 *Phys. Rev. Lett.* **8**, 376.

CAMAC, M. & KEMP, N. H. 1963 *A.I.A.A. Paper* no. 63-460.

CHAN, Y. Y. 1971 *C.A.S.I. Trans.* **4**, 108.
CHUNG, P. M. 1963 *Phys. Fluids* **7**, 110.
CHUNG, P. M. & MULLEN, J. F. 1963 *A.I.A.A. Paper* no. 63-161.
CRANDALL, S. H. 1955 *Quart. Appl. Math.* **13**, 318.
DOUGLAS, J. 1956 *Pacif. J. Math.* **6**, 35.
DOUGLAS, J. & JONES, B. F. 1963 *SIAM J.* **11**, 195.
ENEMOTO, Y. 1973 *J. Phys. Soc. Japan* **35**, 1228.
EU, B. C. & LIU, W. S. 1975 *J. Chem. Phys.* **63**, 592.
FAY, J. A. 1962 *Amp.* 71, *Avco/Everett Res. Lab. Rep.*
FAY, J. A. & KEMP, N. H. 1965 *J. Fluid Mech.* **21**, 659.
FINSON, M. L. & KEMP, N. H. 1965 *Phys. Fluids* **8**, 201.
GLASS, I. I. & LIU, W. S. 1978 *J. Fluid Mech.* **84**, 55.
GLASS, I. I., LIU, W. S. & TANG, F. C. 1977 *Can. J. Phys.* **55**, 1269.
HINNOV, E. & HIRSCHBERG, J. G. 1962 *Phys. Rev.* **125**, 795.
HOFFERT, M. I. & LIEN, H. 1967 *Phys. Fluids* **10**, 1769.
HONMA, H. & KOMURO, H. 1976 *A.I.A.A. J.* **14**, 981.
JAFFRIN, M. Y. 1965 *Phys. Fluids* **8**, 606.
KNÖÖS, S. 1968 *J. Plasma Phys.* **2**, 207.
KUIPER, R. 1968 *Stanford Univ. Rep.* SUDAAR 353.
LIU, W. S. 1978 *Inst. Aerospace Stud., Univ. Toronto Rep.* UTIAS 8 226.
MANSFELD HUTTEN, C. B. L. 1976 Ph.D. thesis, Eindhoven University of Technology, Eindhoven, The Netherlands.
MIRELS, H. 1966 *Phys. Fluids* **9**, 1907.
NISHIDA, M. & MATSUOKA, K. 1971 *A.I.A.A. J.* **9**, 2117.
PARK, C. 1964 *A.I.A.A. J.* **2**, 169.
PETSCHEK, H. & BYRON, S. 1957 *Ann. Phys.* **1**, 270.
SELLS, C. C. L. 1966 *Roy. Aircraft Estab. Tech. Rep.* no. 66243.
SHERMAN, A. & RESHOTKO, E. 1969 *A.I.A.A. J.* **7**, 610.
SU, C. & LAM, S. H. 1963 *Phys. Fluids* **6**, 1479.
TAKANO, Y. & AKAMATSU, T. 1975 *Mem. Faculty Engng, Kyoto Univ., Japan* **36**, 333.
TAMBOUR, Y. & GAL-OR, B. 1977 *Phys. Fluids* **20**, 880.
TSENG, R. C. & TALBOT, L. 1971 *A.I.A.A. J.* **9**, 1365.
WHITTEN, B. T. 1977 Ph.D. thesis, Institute for Aerospace Studies, University of Toronto.
ZAPESOCHNYI, I. P. & FELTSAN, P. V. 1966 *Opt. Spectrosc.* **20**, 291.

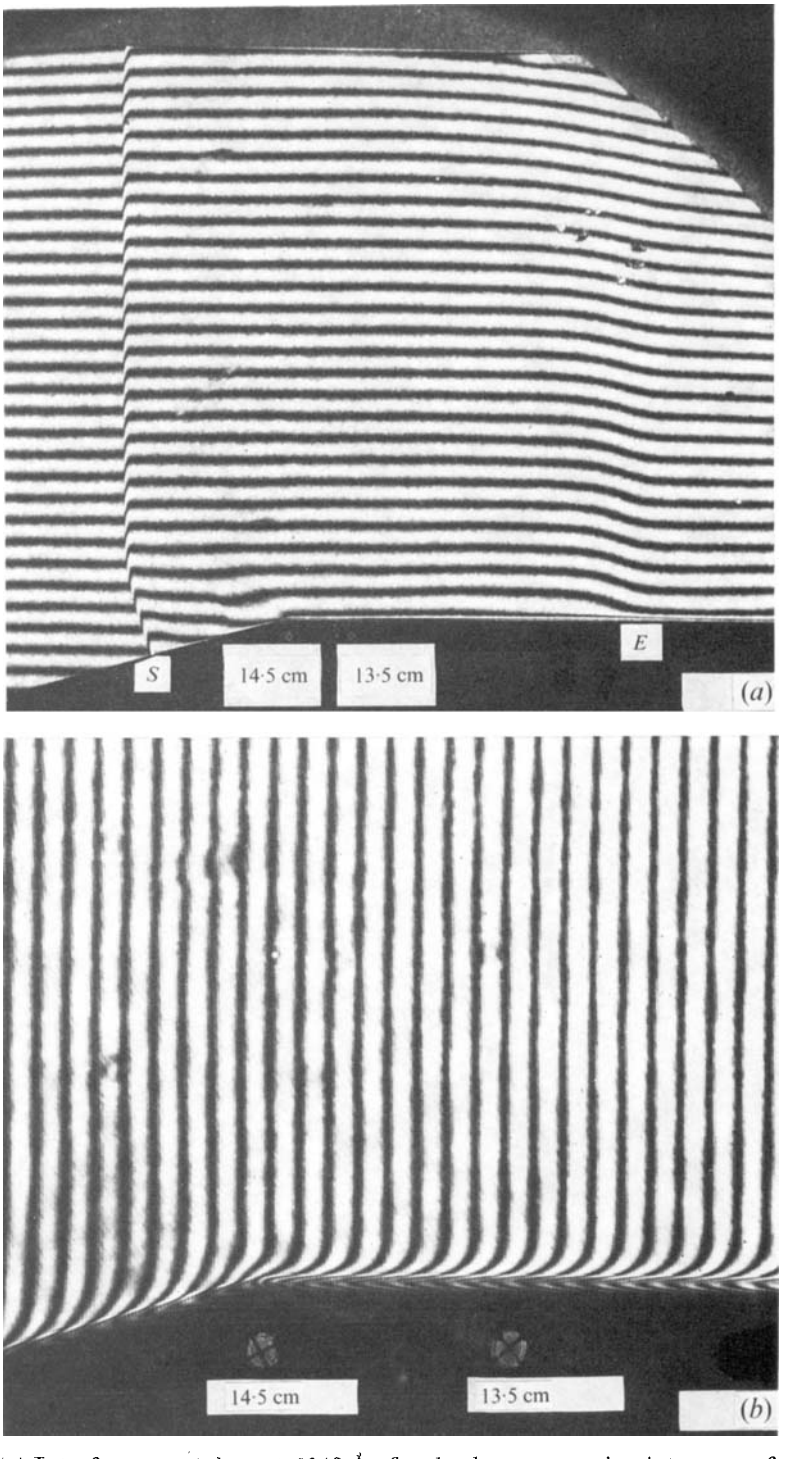

FIGURE 3. (*a*) Interferogram taken at 6943 Å of a shock wave moving into argon from right to left at $M_s = 12{\cdot}8$, $p_0 = 5{\cdot}01$ torr, $T_0 = 297$ °K. The shock wave is diffracting over a 15° sharp-expansion corner. *S*, translational shock wave; *SE*, relaxation zone (10·4 cm); *E*, electron cascade front. At $x = x_E$ (only), $M_E = 1{\cdot}96$, $T_{eE} = T_{aE} = 1{\cdot}13 \times 10^4$ °K, $\rho_E = 6{\cdot}09 \times 10^{-5}$ g/cm^3, $n_{eE} = 5{\cdot}09 \times 10^{16}$/cm^3, $\alpha_E = 0{\cdot}056$, $p_E = 1132$ torr, $u_E = 3376$ m/s, $a_E = 1722$ m/s. (*b*) Interferogram taken at 6943 Å of a boundary-layer flow for the initial conditions in (*a*), 14 cm from the leading edge of the flat plate. The actual inviscid flow conditions resulting from radiation cooling are given in table 1 (case 2).

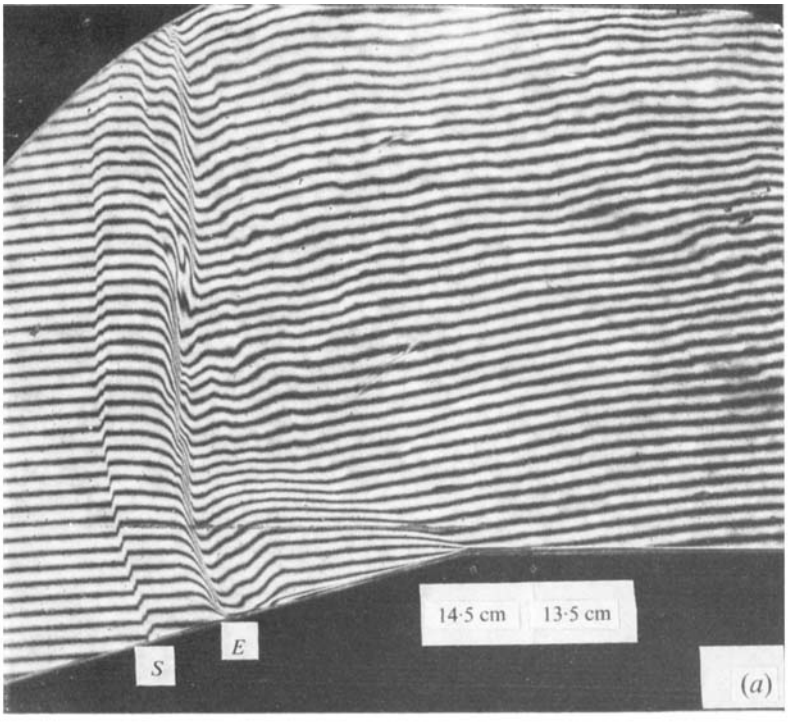

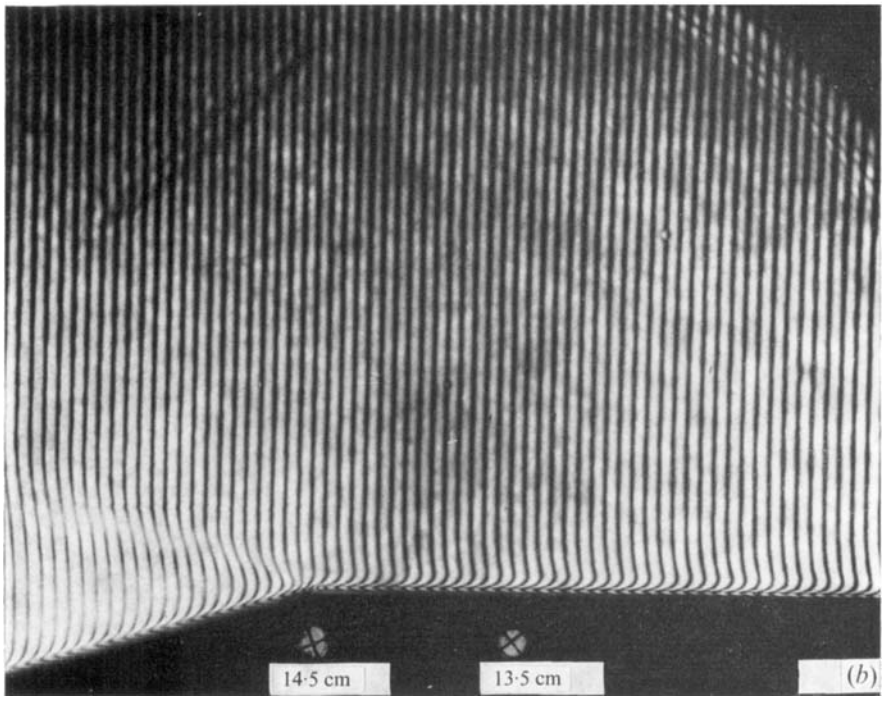

FIGURE 4. (*a*) Interferogram taken at 6943 Å of a shock wave moving into argon from right to left at $M_s = 16{\cdot}6$, $p_0 = 4{\cdot}81$ torr, $T_0 = 296$ °K. The shock wave is diffracting over a 15° sharp-expansion corner. *S*, translational shock wave; *SE*, relaxation zone (1·7 cm); *E*, electron cascade front. At $x = x_E$ (only), $M_E = 2{\cdot}40$, $T_{eE} = T_{aE} = 1{\cdot}31 \times 10^4$ °K, $\rho_E = 8{\cdot}11 \times 10^{-5}$ g/cm^3, $n_{eE} = 1{\cdot}96 \times 10^{17}$/cm^3, $\alpha_E = 0{\cdot}16$, $p_E = 1931$ torr, $u_E = 4639$ m/s, $a_E = 1929$ m/s. (*b*) Interferogram of a boundary-layer flow taken at 6943 Å for the initial conditions in (*a*), 14·0 cm from the leading edge of the flat plate. The actual inviscid flow conditions resulting from radiation cooling are given in table 1 (case 1).